Advances in Superconducting Single-photon Detectors

Kyle DeBry

The Ohio State University Department of Physics

Dr. Gregory Lafyatis (advisor)

Dr. Daniel Gauthier

April, 2020

Abstract

Superconducting single-photon detectors can detect photons from the UV to the infrared with quantum efficiencies above 90% and greater than MHz count rates. They consist of narrow, thin wires of superconductor biased near their critical current. When these wires absorb a photon, part of the wire stops superconducting and becomes resistive. This transition and sudden jump in resistance is what enables the detection of the photon. Over the past two decades, these devices have matured greatly as a technology and have found many applications ranging from quantum optics to astronomy. However, there are still multiple theories of the dominant mechanism behind these devices. Recently proposed theories suggest a more complicated but potentially more powerful detection mechanism, and experiments are only recently starting to demonstrate this effect and its potential applications.

In this research, the capability to fabricate these intricate devices was developed. This requires high-quality deposition of the superconductors, precise machining of the devices with electron beam lithography, and accurate etching of the films. Many parts of the process have been characterized. Additionally, two new directions are being explored. The first attempts to exploit the recently proposed detection mechanism to make detectors with much wider wires, leading to faster detection rates. The second is the fabrication of superconducting single-photon detectors directly onto optical fibers, eliminating the need for complicated coupling structures and alignment of the detector with the fiber.

Contents

List of Figures

List of Tables

Acknowledgments

Thank you to Professors Gregory Lafyatis and Daniel Gauthier for their support and guidance. Additionally, thank you to Kathryn Nicolich for all her help and advice, and Aimee Price for her help with all things nanofabrication.

This thesis has been supported by the College of Engineering Undergraduate Research Scholarship.

1 Introduction

Many experiments, ranging from astronomy to quantum optics, require the detection of individual photons by single-photon detectors. The two main types of single-photon detectors, single-photon avalanche diodes (SPADs) and superconducting nanowire single-photon detectors (SNSPDs), each have advantages and disadvantages. In the telecom regime around 1550 nm, SNSPDs are useful tools in situations requiring high quantum efficiency ($> 80\%$) detection of infrared photons and relatively high speeds ($> 1\,\mathrm{MHz}$) [1, 2]. Applications include interferometry experiments, quantum key distribution, and astronomical observations. However, both the efficiency and speed of SNSPDs can limit some experiments, and so it is desirable to continue improving the state-of-the-art.

Over the last four years, I have developed the procedures we use to fabricate superconducting single-photon detectors. This process requires high quality deposition of the superconductors, precise nanofabrication with electron beam lithography, controlled etching, and the ability to wire bond to the finished devices. Fabricating these devices is a difficult process that only a handful of groups around the world are able to do, and having this foundation will allow the group to explore new avenues of research into the physics and engineering of single-photon detectors.

Additionally, I have begun to explore two interesting directions for building on this capability. First, I have been investigating the possibility of using wider wires in the superconducting single-photon detectors using a recently theorized detection mechanism. These detectors have a substantially higher detection rate and could lead to further discoveries in the physics of these devices. We are currently on the last stage of process development before having a test device of this type.

The other direction I have been looking at is the possibility of integrating the superconducting single-photon detector directly onto an optical fiber, instead of fabricating it on a wafer and coupling a fiber to that. This could lead to even higher quantum efficiencies with strong coupling, and could potentially decrease the complexity of the fabrication pro-

cess by removing the need to align the fiber with the detector. I have carried out numerical simulations to asses the detection efficiency of various designs and started working towards fabricating proof-of-concept devices.

1.1 Superconductivity

Superconductors area a class of materials that have no resistance and reject magnetic fields when they are below their critical temperature, T_c, where there is a sharp transition. First observed in pure metals like mercury, superconductivity is now known to exist in a broad class of materials with many different structures. In this group, we primarily work with two superconductors, niobium nitride (NbN) and an amorphous alloy of molybdenum and silicon known as MoSi (pronounced "moh-see"). MoSi is also sometimes denoted Mo_xSi_{1-x}, where x is the fraction of the material made of molybdenum. Typical values for x are around 70%-90%. MoSi thin films have a critical temperature of 6-8 K [3], while NbN films can have critical temperatures as high as 16 K [4, 5, 6]. Critical temperature measurements of both materials are shown in Figure 1, where this sample of MoSi has a critical temperature (half maximum) of just over 6 K, and this sample of NbN has a critical temperature of near 8 K. For very thin films, the transition temperature tends to decrease significantly from the bulk transition temperature [7].

For our purposes, there are a few other properties of superconductors that are especially interesting. First, the charge carriers in superconductors are Cooper pairs, which are pairs of electrons with equal and opposite momentum and spin. They are bound together through interactions between the electrons and phonons of the material. According to the BCS theory of superconductivity, there is an energy gap $\Delta(T = 0) = 1.764 k_B T_c$, where k_B is the Boltzmann constant. This is the energy required to break a Cooper pair when the temperature is well below the critical temperature, which is the regime single-photon detectors operate in [8, p. 63]. Additionally, there is some material-dependent "deparing" current I_{dep} at which the magnetic field created by the current is strong enough to break apart the

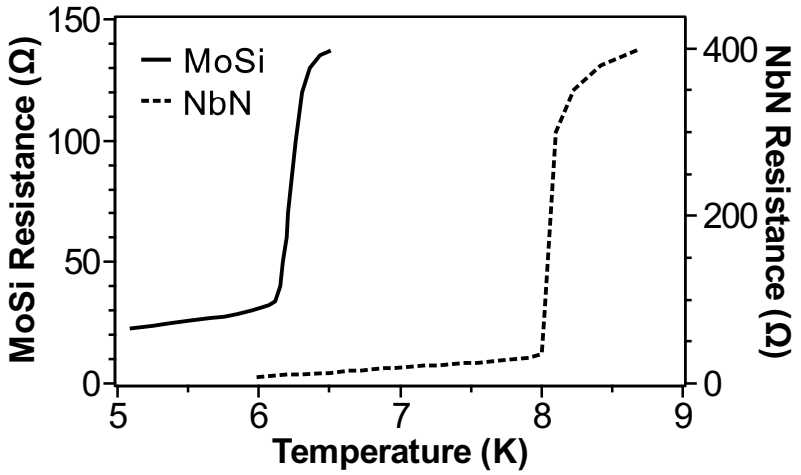

Figure 1: The resistance versus temperature curves of a thin film sample of MoSi and another thin film sample of NbN, showing their critical temperatures. These measurements were made in our cryostat on films we deposited, which were roughly 1 mm long and 3 mm wide.

Cooper pairs. This depairing current is often much greater than the geometry-dependent "switching" current I_{sw}, which is the current at which the superconductor becomes normal in practice. There are many causes for a low I_{sw}, including physical roughness, bottlenecks, and current "pinching" around sharp corners. The switching current is determined by the weakest point in the wire, requiring the entire wire to be highly uniform for a high I_{sw}. In the standard "hot spot" model of superconducting single-photon detectors, a detection event occurs when a photon is absorbed by the superconductors with sufficient energy to break enough Cooper pairs to turn a section of the superconductor normal.

Other properties of superconductors useful for other applications include that their electrical conductivity and their thermal conductivity are not linked via the Wiedemann-Franz law in the same way other metals are [9], and so they can be used to conduct electrical signals at low temperatures without putting a large thermal load on the coldest parts of a system [10].

1.1.1 Amorphous superconductors

In the traditional study of superconductivity, crystalline structures are considered that have high symmetry, leading to straightforward mathematical representation of the phonons and electrons in the material. This is the context in which the BCS theory of superconductivity was first formulated [8, p. 44]. However, amorphous (non-crystalline) materials became a subject of interest in the late 20th century [11, p. 162] after the first observation of superconductivity in amorphous bismuth in 1954 [12]. In many materials, including MoSi, the transition temperature in the superconducting state can be several times higher than in the crystalline state. For MoSi, the amorphous phase has a T_c of ~ 7.5 K, while the crystalline phase has a T_c of only ~ 1.4 K [13, p. 741].

Our particular amorphous material of interest, Mo_xSi_{1-x}, superconducts when $x > 18\%$ [14]. MoSi is a promising material for superconducting nanowire single-photon detectors due to high detection efficiency at a higher critical temperature than other similar materials [15], with a maximum T_c of 7.6 K with a composition of $Mo_{83}Si_{17}$ [16]. Because the energy gap Δ is low relative to its thin film transition temperature compared to other materials, MoSi has the potential for high performance at temperatures above 1 K [7]. For example, the superconductor WSi has a much lower transition temperature when in thin film form than MoSi but a similar band gap. However, presently most studies of superconducting single-photon detectors focus on NbN and WSi.

1.2 Superconducting nanowire single-photon detectors

Superconducting nanowire single-photon detectors (SNSPDs) are based on long, thin superconducting wires that become normal when it absorbs a photon [18]. The superconducting nanowire is biased with a current close to the switching current, and when the photon is absorbed by it (Fig. 3a), it breaks cooper pairs and decreases the local critical current, causing creating a non-superconducting (normal) region called a "hot spot," shown in Fig. 3b. This hot spot causes the current to be redirected around itself, increasing the current density on

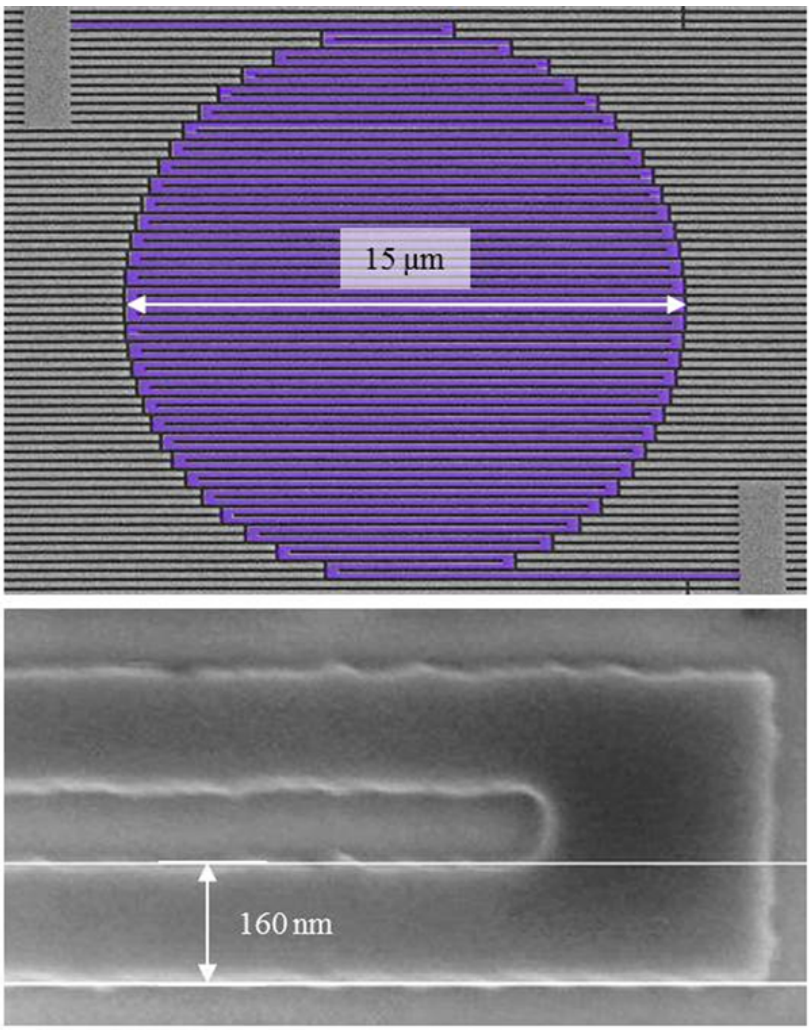

Figure 2: A scanning electron micrograph of an SNSPD (top) and the nanowire comprising the SNSPD (bottom), from [17].

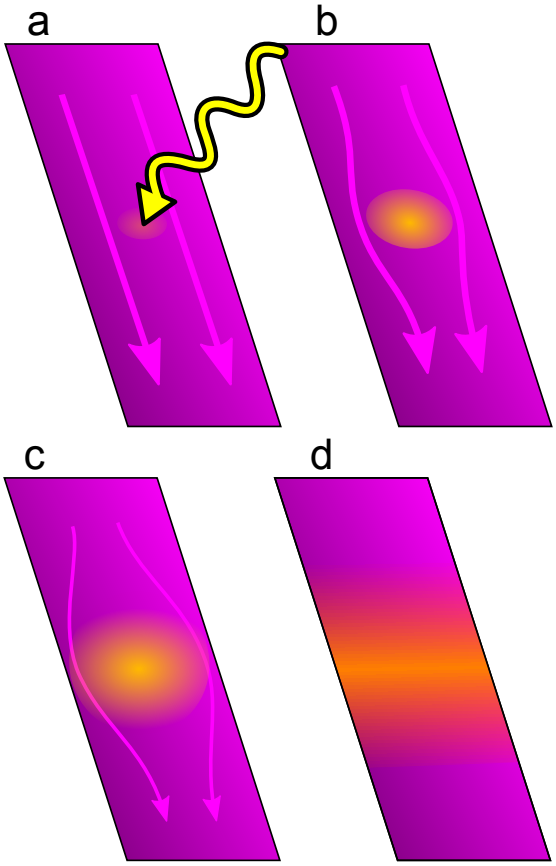

Figure 3: A schematic depiction of the hot spot theory of photon detection: (a) a photon strikes the nanowire and is absorbed; (b) the photon breaks Cooper pairs causing a small hot spot to form; (c) the hot spot diverts the current to the edges of the nanowire, increasing the local current density above the critical current; (d) the entire nanowire becomes resistive and shunts current to the amplifier. Here, the width of the wire is approximately 100 nm.

either side of the hot spot to above the critical current, shown in Fig. 3c. For a detection event, the entire width of the wire must become normal, seen in Fig. 3d.

These hot spots were first described in [19], and applied to single photon detection in [20]. The thin films we are interested in are described by a thickness d, heat capacity C, thermal conductivity κ, and electrical conductivity σ. Additionally, there is a heat transfer coefficient per unit area α between the film and the substrate, which is held at temperature T_0. The heat flow equation is then [20]

$$Cd\frac{\partial T}{\partial t} = \kappa d\nabla^2 T + \alpha(T_0 - T). \tag{1}$$

This then has a characteristic thermal relaxation time $\tau = Cd/\alpha$ and a thermal healing length $\Lambda_{th} = (\kappa d/\alpha)^{1/2} = (D\tau)^{1/2}$, where $D = \kappa/C$ is the thermal diffusivity [19]. If a photon with energy $\hbar\omega$ is absorbed, Eq. 1 has the solution

$$T(r,t) = T_0 + \frac{\Theta}{t}e^{-t}e^{-r^2/4t}, \tag{2}$$

with t in units of τ and r in units of Λ_{th}. The characteristic temperature increase Θ has a value of $\hbar\omega/(4\pi\Lambda_{th}^2 Cd)$. Taking these characteristic values leads to the approximation that the average temperature increase inside a radius of $2\Lambda_{th}$ on the timescale of τ is approximately Θ [20]. Typical values of Λ_{th} for an NbN film with $d = 6\,\text{nm}$ are around 10 nm to 20 nm [18], meaning that the hot spot would have a diameter of $4\Lambda_{th} \approx 40\,\text{nm}$ to 80 nm. This is what sets the maximum width of the wire for SNSPDs and leads to detectors with wires that are roughly 100 nm wide. Additionally, this is also restricts d, because Λ_{th} depends on d (through the thermal relaxation time τ). In order for Λ_{th} to be large enough for the devices to be fabricated, d must be only a few nanometers.

Once the hot spot encompasses the full width of the wire, its total resistance is still small. This normal region then expands along the length of the nanowire through Joule heating until the resistance is very large, often a MΩ or more. The dead time of an

SNSPD after detecting one photon before it can detect another is determined by its kinetic inductance [21], which comes from the inertia of the Cooper pairs in the superconductor. It is proportional to the length of the superconducting wire and inversely proportional to its cross sectional area. Because most SNSPDs have long, thin, narrow wires, they generally have high kinetic inductances, leading to comparatively long dead times on the order of 100 ns.

SNSPDs are part of a larger circuit consisting of a current source, a bias-tee, an amplifier, and the SNSPD. The bias-tee is oriented so that DC current flows from the current source to the detector, but AC signals go from the detector to the amplifier. When there is not a detection, the current flows through the near-zero resistance SNSPD to ground. When a detection occurs, however, the SNSPD becomes highly resistive. Because of this, the current is shunted through the AC arm of the bias-tee to the amplifier, where it is detected as a voltage pulse. Then, during the reset period, the current returns to the SNSPD.

SNSPDs were first predicted in 1996 [20] and demonstrated in 2001 [22], using a very simple device made of NbN. Over the next two decades, SNSPDs have become a dominant single-photon detection technology due to their high detection efficiency at telecommunication wavelengths (1550 nm). By carefully designing an optical cavity around the SNSPD, system detection efficiencies of 98% have been demonstrated [23]. Although SNSPDs typically only measure that one or more photons were detected with no indication of the exact number, our group showed recently that standard SNSPDs are capable of photon number resolving detection [24, 25].

Two important limitations of traditional SNSPDs are their large kinetic inductance, and their need to be optically coupled to a fiber. The longer reset times of most SNSPDs due to their high kinetic inductance can be a limitation in some experiments as the prohibit high count rates. Additionally, on their own, bare SNSPDs do not detect a very high fraction of the light ($< 50\%$) that passes through them. To address this, optical cavities made of Bragg reflectors are built around the SNSPDs. These optical cavities cause the photons

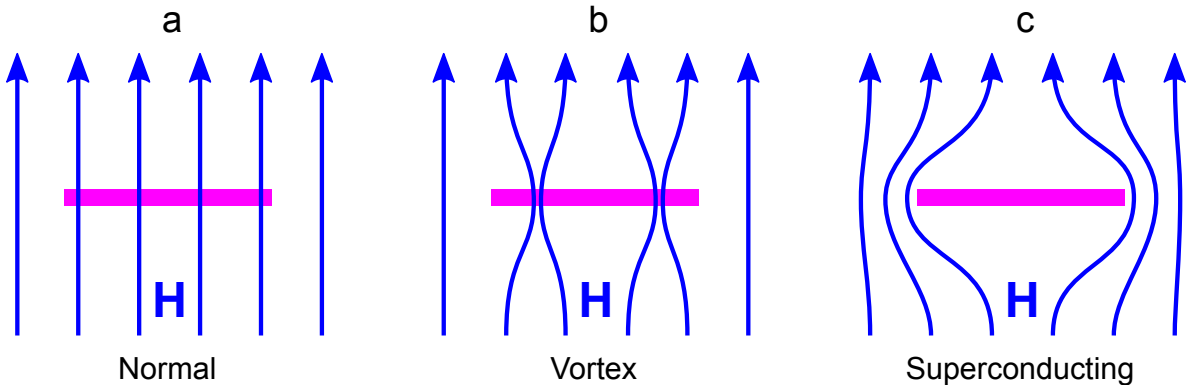

Figure 4: Edge-on view of a thin film of superconductor (purple) in a magnetic field under various conditions. The magnetic field responds to three states of a type-II superconductor: (a) the normal state, where $T > T_c$ or $H > H_{c2}$; (b) the vortex state where $H_{c1} < H < H_{c2}$; (c) the fully superconducting state where $H < H_{c1}$ and the material behaves like a type-I superconductor.

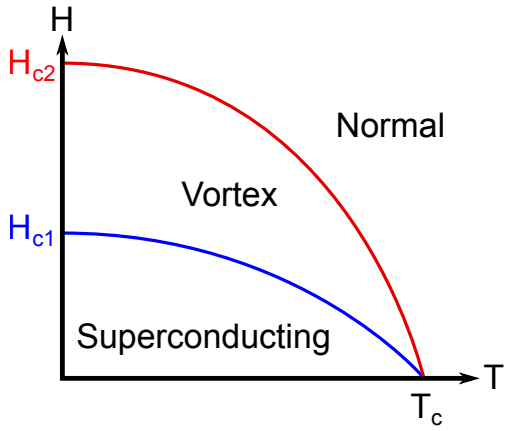

Figure 5: A temperature versus magnetic field plot for a type-II superconductor showing the three possible states: normal, a mixed vortex-penetrated state, and fully superconducting.

to effectively pass through the SNSPDs many times, leading to high system efficiencies. However, they only function near the resonance of the Bragg reflector, so an individual SNSPD is only useful in a very small wavelength range. Additionally, the alignment of the fiber to the detector requires lining up the ∼8 µm core of the fiber with the ∼15 µm active area of the SNSPD [26].

1.3 Bridge detectors

Another interesting property of superconductors is the well-studied phenomenon of the formation, pinning, and drift of vortices. In type-II superconductors, such as NbN and MoSi, there are two critical fields, $H_{c1} < H_{c2}$. Above H_{c2}, superconductivity is destroyed (Fig. 4a), and below H_{c1} the material acts like a typical type-I superconductor by expelling all magnetic field (Fig. 4c). In between the two critical fields, however, magnetic flux lines can penetrate the material, as shown in Fig. 4b. The relationship between these three states is plotted in Fig. 5. The sites where the lines penetrate the superconductor are known as magnetic vortices, and each carries one quantum of magnetic flux Φ_0 and angular momentum $\hbar$. These magnetic vortices are subject to Lorentz forces $\boldsymbol{J} \times \boldsymbol{\Phi_0}/c$, and if not pinned strongly enough, they will move across the superconductor transversely to the direction of the current flow. This phenomenon has been observed directly in MoSi [27], as well as many other type-II superconductors. If they move with velocity $\boldsymbol{v}$, this induces and electric field $\boldsymbol{E} = \boldsymbol{\Phi_0} \times \boldsymbol{v}/c$ opposed to the current that acts as a resistive voltage, leading to Joule heating [8, p. 163]. Absorbed photons are also capable of creating vortices in addition to any equilibrium distribution of vortices, and these additional vortices will move and cause Joule heating of the superconductor. This is the basis for the theory of micron-scale superconducting single-photon detectors.

However, to fully understand this phenomenon, one must use a more complete picture of superconductivity. The best theory we have currently is the time-dependent Ginzberg-Landau (TDGL) theory [8, p. 399], although this theory is only valid neat T_c. As these devices are operated in practice well below T_c, it is important to view these results with some skepticism. TDGL theory was first applied to superconducting nanowire single-photon detection in 2012 [28]. Then in 2017, Vodolazov *et al.* [29] suggested that the vortices created by incident single-photons could be used to detect photons in new ways. Specifically, they showed that when the bias current is large enough, the strong dependence of detection efficiency on the width of a nanowire disappears, allowing for much wider wires to detect

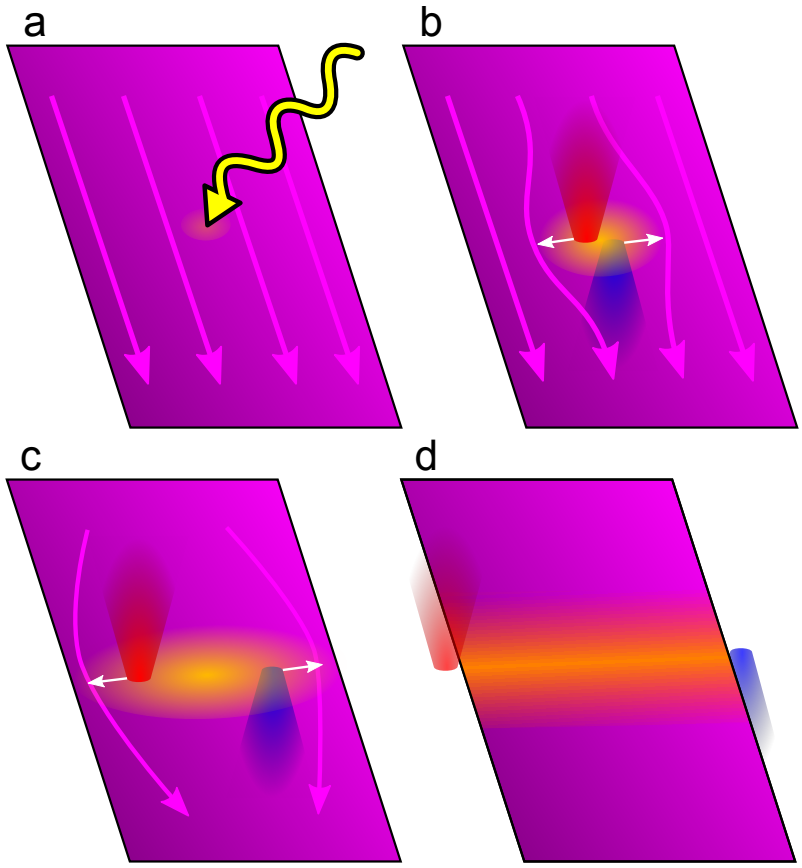

Figure 6: A schematic depiction of the vortex theory of photon detection: (a) a photon strikes the wire and is absorbed; (b) the photon creates a magnetic vortex-antivortex pair; (c) the vortex and antivortex move towards opposite edges of the wire, turning the material normal as they move; (d) the entire wire becomes resistive and shunts current to the amplifier.

photons with the same efficiency as narrow wires. This is in contrast to the hot spot model, where the heating is local and causes a strong dependence of the detection efficiency on the width of the wire.

In the vortex model, the length scale that dictates the maximum width of the wire is the Pearl length $\Lambda = 2\lambda^2/d$, where λ is the London penetration depth and d is the thickness of the film [29, 30]. In NbN, the London penetration depth is $\lambda \approx 470\,\text{nm}$ [31], leading to a Pearl length of $\Lambda \approx 70\,\mu\text{m}$ for a 6 nm thick film, compared to the thermal healing length $\Lambda_{th} \approx 15\,\text{nm}$ for the same film that sets the length scale of hot spots, limiting the width of SNSPDs.

The process of detecting a photon is depicted in Fig. 6, which shows how the vortices and antivortices created when a photon is absorbed travel to the edges of the wire, creating a normal strip that spans the wire. This mechanism was first demonstrated in practice the in 2018 with an NbN wire approximately 2 microns wide [30]. These larger "bridges" of superconductor are still being explored and are a ways off from any practical application. The first experimental evidence of this in an amorphous superconductor, specifically MoSi, was only published in spring of 2020, and is shown in Fig. 7 [32]. There is still a great deal to learn about this mechanism.

This phenomenon occurs specifically when the bias current is at least some fraction of the depairing current I_{dep}, which changes depending on temperature and the wavelength of the photons but range from $0.5I_{dep}$ to nearly $1I_{dep}$ for typical parameters [30]. These values are determined numerically, but the high current is required to produce a stronger magnetic field at the surface of the superconductor, putting it in the "vortex" region of Fig. 5. Many modern detectors only have switching currents near 60% of I_{dep} [33], so improvements in the material characteristics and fabrication accuracy may be needed. We hope that an improved deposition chamber and careful lithography will enable us to make bridge detectors that can detect photons with high efficiency.

My work in this area has been to develop pattern designs for fabricating bridge

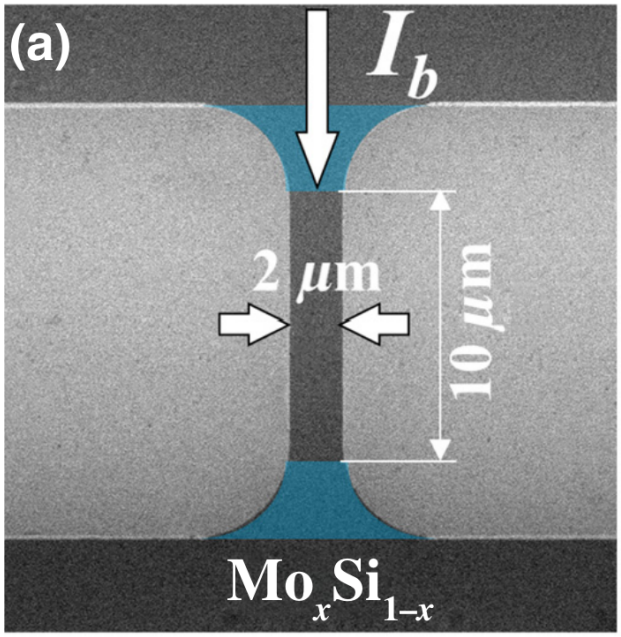

Figure 7: An experimentally demonstrated bridge detector made of MoSi, from [32].

detectors and experimentally find the correct electron beam lithography dose. We are nearly ready to begin testing these devices.

2 Fabrication

For SNSPDs and other superconducting single-photon detectors to function, they require the bias current to be close to the switching current, or even to the depairing current, at every location along the superconducting wire that can detect photons. This requires the wire to be extremely uniform in width, thickness, and composition, as variations in any of these parameters will alter the switching and depairing currents at different positions along the wire, and the bias current is limited by the minimum switching current for the entire wire. This requirement of extreme uniformity is what drives all of our decisions regarding the deposition and fabrication of our devices. We deposit the films through ultra-high vacuum (UHV) sputtering, and use electron beam lithography (EBL) to pattern the devices.

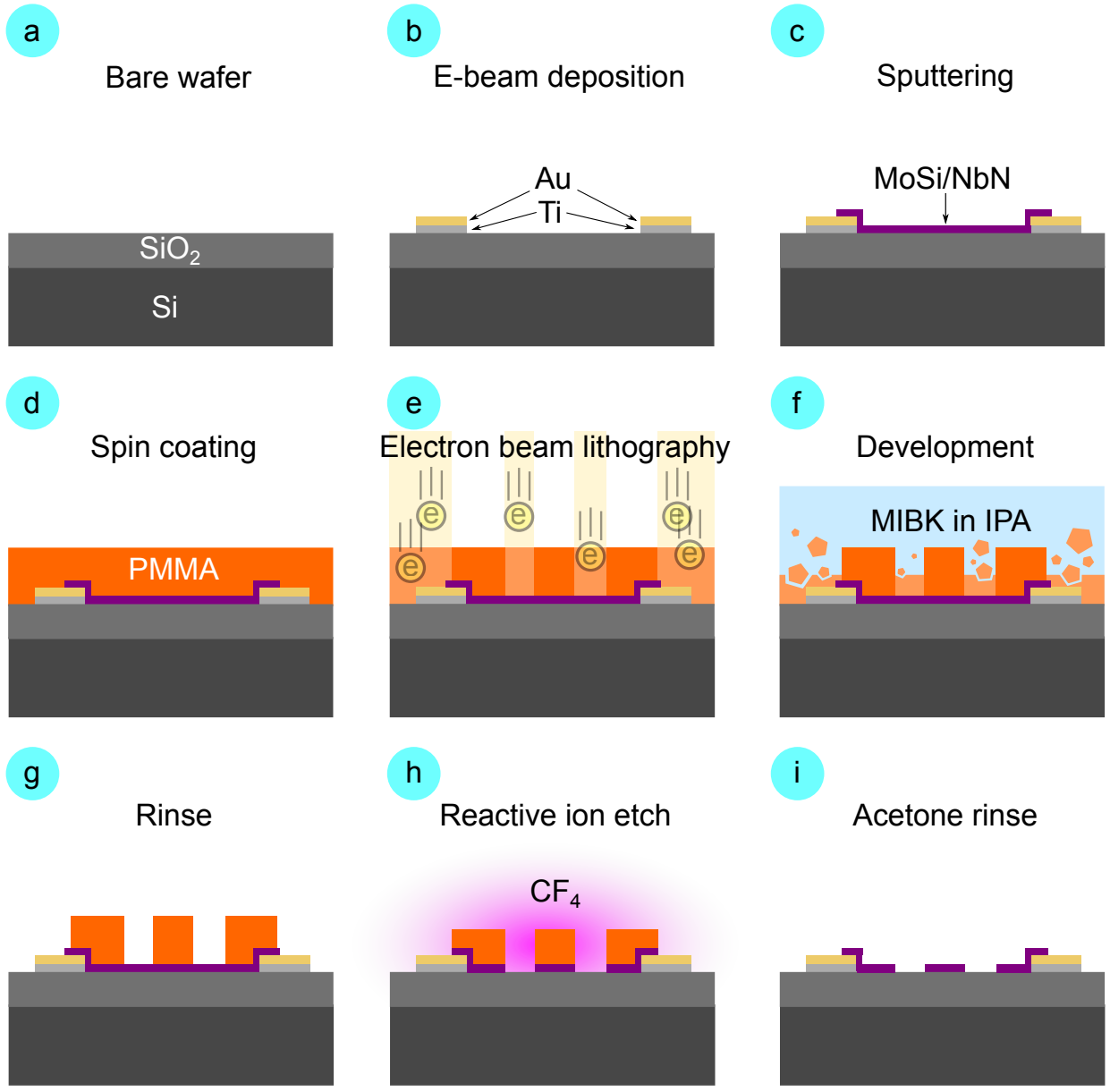

Figure 8: Depiction of the full nanofabrication process: (a) bare wafer; (b) electron beam evaporation of gold and titanium; (c) sputtering deposition of superconductors; (d) spin coating with PMMA; (e) electron beam lithography exposure; (f) development of PMMA in MIBK; (g) resulting structure in PMMA; (h) etching the exposed superconductor using RIE; (i) completed superconducting single-photon detector.

2.1 Overview

The fabrication of SNSPDs and bridge detectors is a complicated processes that takes multiple workdays to complete. Figure 8 gives an overview of our current process by examining a cross section of a device as it is fabricated, starting with a bare wafer. Our current wafers are 2 inches in diameter and 250 microns thick, capped with a layer of silicon dioxide, as shown in Fig. 8a. Then, as shown in Fig. 8b, we deposit electrical contacts by evaporating metals using an electron beam evaporator system. Gold deposited directly onto SiO_2 does not adhere well, so 10 nm of titanium is used as a sticking layer, followed by 50 nm of gold. The shape of the contacts is determined by a physical aluminum mask placed over the sample during deposition. Next, DC or RF magnetron sputtering [34] is used to deposit a thin film of the superconductor, which is either MoSi or NbN in our case, as shown in Fig. 8c. Again, a physical mask is used to control the location of the deposition, and the films are less than 10 nm thick.

Samples are taken to the nanofabrication facility Nanotech West (NTW), where the nanoscale patterning takes place. First, a few hundred nanometers of an electron beam resist is coated onto the sample using a spin coater (Fig. 8d). In this case, the resist is poly(methyl methacrylate) or PMMA, which is chemically the same as acrylic. The reason that PMMA is effective as an electron beam resist is that, when it is exposed to high-energy electrons, the polymer bonds that hold its structure together are broken, allowing those regions of the resist to be removed [35]. This is where the electron beam lithography system comes in, as the machine's purpose is to expose regions of a sample to high energy electrons (50 kV or 100 kV) with precision of 10 nm or better, as depicted in Fig. 8e. This is what allows us to write the intricate patterns necessary for SNSPDs, and to write patterns with high enough precision for the bridge detectors to function. Then, the areas of the resist that were exposed can be removed using the developer methyl isobutyl ketone (MIBK) diluted in isopropyl alcohol (IPA) as shown in Fig. 8f. This leaves behind PMMA that is patterned into the shape we want our detectors to have (Fig. 8g), but this must still be transfered to

the superconductor.

To transfer the pattern to the superconductor, it is brought back to the NSL cleanroom. There, we use reactive ion etch (RIE) to etch the sample. Reactive ion etching creates a chemically reactive plasma (in our case CF_4) that eats away at both the superconductor and the resist (Fig. 8h). However, because the resist is so much thicker than the superconductor, and because of the etch rates of the different materials, the superconductor is etched through long before the resist is depleted. Finally, PMMA has the nice property that it can be removed simply by rinsing with acetone (followed by IPA as always), leaving behind only the superconductor in the desired shape (Fig. 8i).

2.2 Deposition

I will summarize the steps we took to get where we are now. All of our samples thus far have been deposited with the Lab18 deposition system in NSL in the PRB. We are concerned with three primary elements: the roughness of the substrate and of the films, the quality of the deposited superconductor, and the thickness of the films. Care is also taken to keep the sample very clean at all times, and it should never be exposed to air outside of a cleanroom until the very end of the process when the detectors are being wire bonded or a test film is being loaded into the cryostat.

Starting with the roughness, we use Si wafers capped with SiO_2 directly from the manufacturer. The roughness of these wafers is within the digitization noise of the AFM available in NSL and is specified as $<0.2\,\text{nm}$ RMS roughness. Then, we use physical deposition masks to deposit our films and gold contacts instead of any optical lithography because the optical lithography may increase the roughness of the wafer's surface before the films are deposited. We have used several different masks over the years, but currently we use the masks shown in Figs. 9-11. These show both the masks for the gold contacts and the masks for the superconductors. The superconducting mask has an extra slot on the left that can be used for characterization, such as X-ray diffraction (XRD) measurements of the thickness

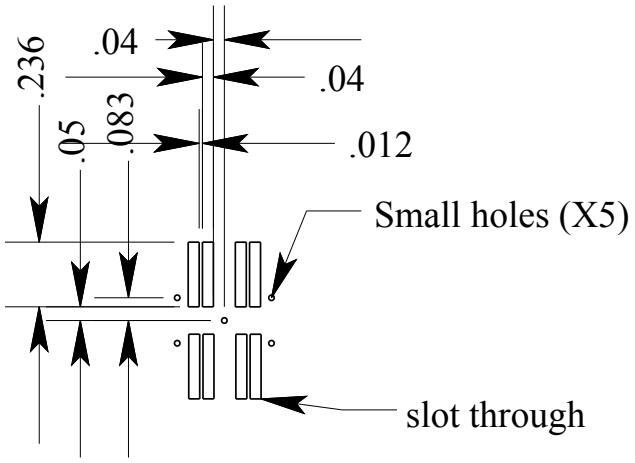

Figure 9: The mask pattern for the gold electrical contacts used in the deposition process. Units are inches.

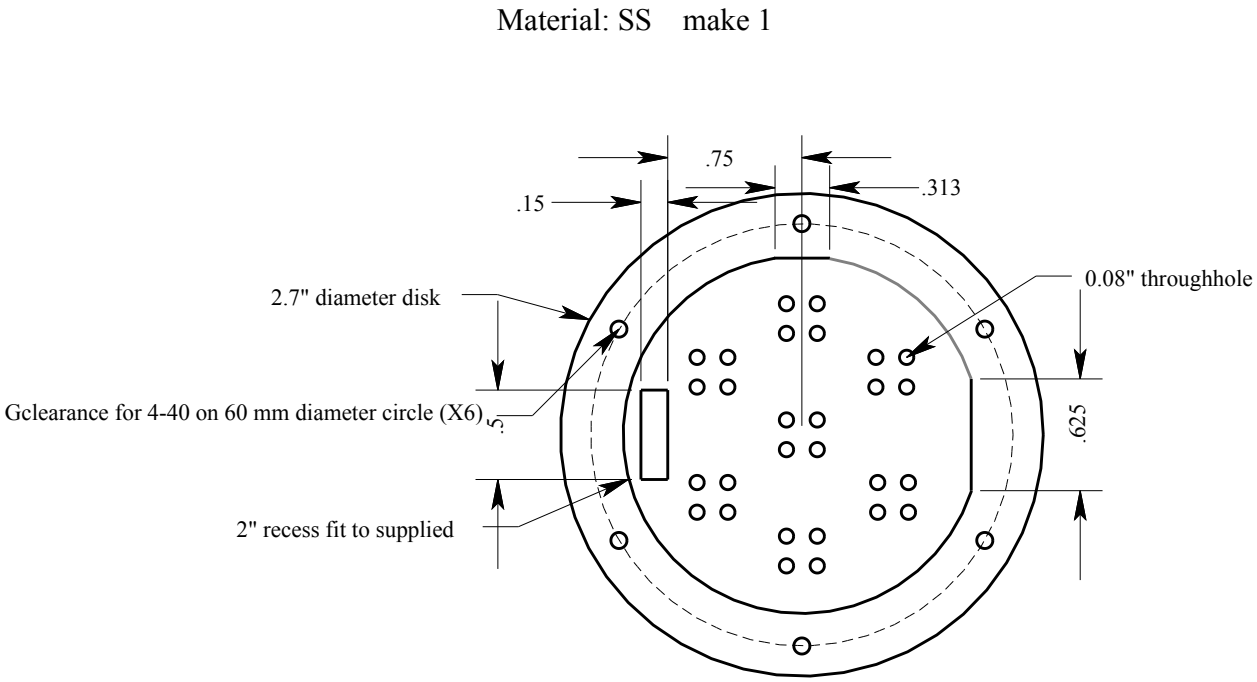

Figure 10: The mask schematic for the superconductor deposition showing the positions of the superconductor films for the seven sets of devices on a wafer, along with a large hole on the left for characterization such as XRD or AFM.

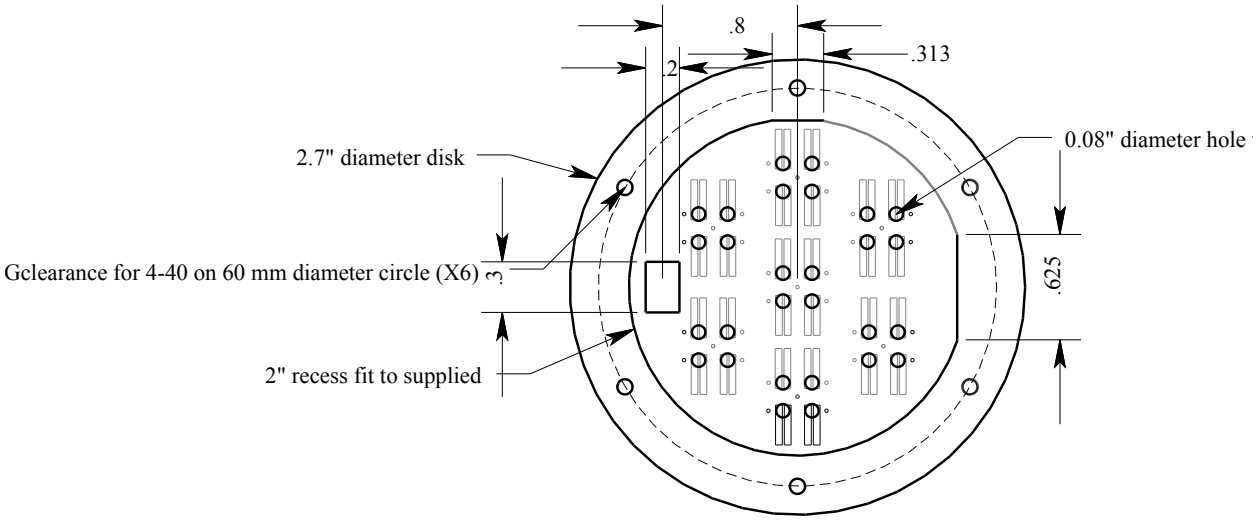

Figure 11: The mask schematic for the both the gold and superconductor masks together, showing the positions of the the seven sets of devices on each wafer and the alignment of the superconducting mask with the electrical contact mask.

of the film, or Energy-dispersive X-ray spectroscopy (EDS) which is available at Nanotech West on SEM02 and can measure the elemental composition of the film (for a thick enough film). By only using these masks for deposition, we hope to keep our samples roughness to near the roughness of the substrate itself. The roughness of the films should be measured occasionally using the AFM to ensure that it has not worsened by changes in the sputtering target or other deposition conditions.

To deposit quality superconductors, we take great care to achieve better vacuums and fast deposition times. Both of these goals do the same thing: decreasing the amount of contamination in the superconductor from other elements or molecules present in the chamber. The better vacuum's contribution is obvious, but a faster deposition rate will leave less time for other particles to land on the substrate during the deposition process. After depositing titanium (as a sticking layer) and gold contacts using the first mask with the electron beam evaporator, MoSi or NbN are sputtered with the second mask. MoSi is co-sputtered with a molybdenum and a silicon sputtering target, using rates calculated from measuring the rate of each individually. NbN is deposited by sputtering niobium in a nitrogen atmosphere. The films are typically between 4 nm and 10 nm thick.

To deposit films of accurate thickness, we trust that the deposition rate at a certain sputtering power is constant over a long time period. By using XRD to measure the thickness of a sample of thick film deposited for a known time duration, we calculate the amount of time needed to deposit a film for a desired thickness, and base our sputtering exclusively on the time it takes. The sputtering chamber does have a thickness gauge, but it is not precise enough for our needs. I have not looked in detail into how the thickness affects performance, but NIST typically uses 4 nm films, based on my conversations with Sae Woo Nam's group in summer 2019. Historically, we have deposited thicker films of 8-10 nm.

There are also other considerations when depositing the films, which I will not go into detail about. One is that it is crucial to prevent the crystallization of the amorphous MoSi films during deposition, and there can be several factors that lead to this [36]. However, the dominant factor for out purposes is likely the temperature of the films during deposition [16]. Crystallization leads to a degradation of the superconducting properties, and specifically a decrease in the transition temperature [13, p. 741].

After depositing the films, it is critically important that they are carefully labeled and kept clean. It is known that MoSi, over a period of weeks or months, will degrade in air, so we store the films under a low vacuum in a box in Physics Research Building room 4115. I also maintain a document recording the conditions of deposition for each film, and the history and use of each of the seven samples made from each wafer.

2.3 Scribing

Typically, because we are interested in rapidly iterating and testing designs, we do not write all 28 samples on a wafer at once. Instead, we will write one (or a few) out of the seven groups of samples at a time, with each group containing four samples. The gold patterns of a single group are shown in Fig. 9. To separate the samples, they are scribed using a diamond tip pen scribe into squares that are roughly 2 cm on a side.

Our wafers are 2 inch diameter, 250 micron thick silicon wafer capped with silicon

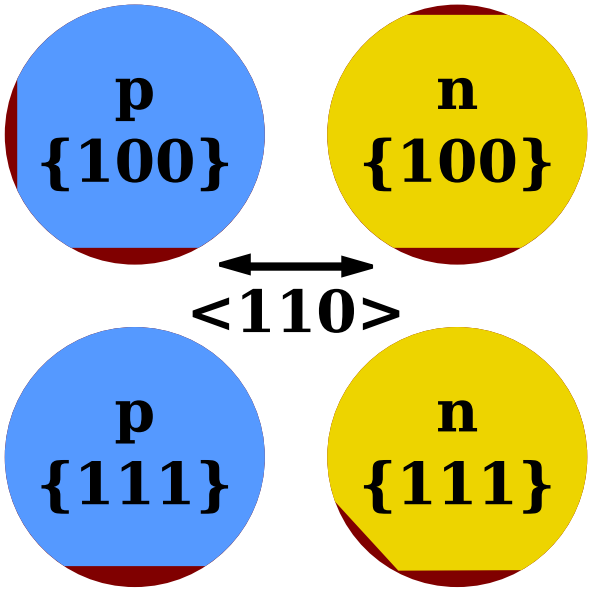

Figure 12: The flat sides of a wafer denote the crystallographic structure and the orientation of the crystal axes [37].

dioxide. Because they are thinner than standard 4 inch wafers, I find that it is easiest to scribe them along a straight edge and simply break the two pieces apart by bending them with my (gloved) hands. Although silicon is one of the easiest materials to scribe and break, it is still best practice to scribe along the crystal axes of the wafer. Figure 12 shows how the flats of a wafer denote the crystallographic structure and axes. Silicon has a face-centered cubic structure, and our wafers have a {100} orientation, with two flats on adjacent sides. To scribe along the crystal axes, scribe parallel or perpendicular to either of the flats using a straight edge. Other wafers, such as GaAs, have different crystal structures and can be much more challenging to scribe into a desired shape. I have used GaAs wafers in the past for energy-dispersive X-ray spectroscopy (see subsection 2.7), and they tend to shatter rather than scribe, due to the crystal structure and orientation.

2.4 Electron beam resist

In order to achieve the tight tolerances required for this level of uniformity, we use electron beam lithography to pattern the films. Our current recipe is based on the recipe used by

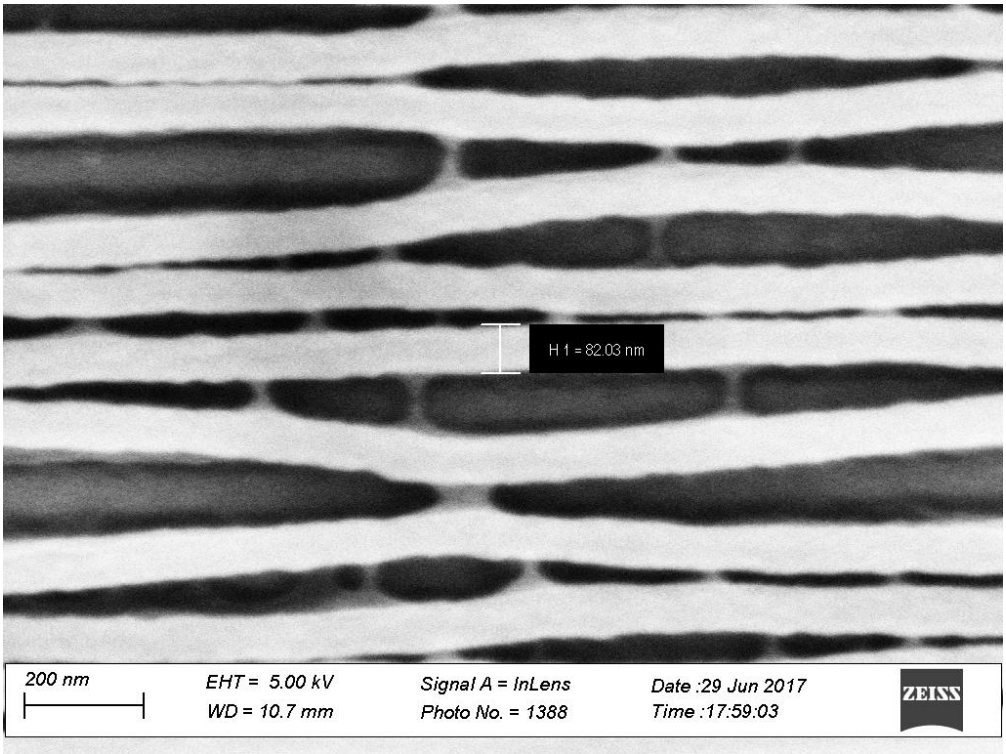

Figure 13: A scanning electron micrograph of lines written in PMMA, showing the poor adhesion and drift of the originally straight lines due to insufficient baking.

the Nam group at NIST, and uses the electron beam resist PMMA. We started with PMMA years ago but had adhesion issues, and switched to the resist hydrogen silsesquioxane (HSQ), trying several different developers. However, we then discovered that the developers were destroying the thin films, and have since returned to PMMA. In this section I will briefly summarize each of these three stages in the development of our process. Georgia Tech has a website that provides a basic overview and spec sheets for a variety of electron beam resists [38].

2.4.1 PMMA with low temperature bake

PMMA is a positive tone resist, meaning that the areas that are exposed are removed during development, and the areas that are not exposed are left behind during development. When we first started, I used PMMA as it was the simplest resist to use. It is polymer-based and not nearly as temperamental as HSQ. However, at the time we were quite worried

about our amorphous MoSi films crystallizing, which can occur at high temperatures and has been shown to worsen the superconducting properties of MoSi by reducing the transition temperature [13]. This is known to happen when it is deposited at high temperatures, but we did not know whether it would also occur if heated later. This meant that we did not want to bake our samples to drive off moisture and promote adhesion, which is the recommended recipe for coating with PMMA. The recommended temperature is 160 °C, but I never heated our samples above 80 °C. This led to extremely poor adhesion, as seen in Fig. 13. The lines in the resist, after being developed, are falling over and moving around on the substrate. This is what led us to move to HSQ.

2.4.2 HSQ

Hydrogen silsesquioxane (HSQ) is a negative tone resist, meaning that the exposed areas will remain during development. Some HSQ recipes do not call for high temperature bakes, which was encouraging as we were trying to limit the temperature our samples reached during the fabrication process. Additionally, the Berggren group at MIT has used HSQ to pattern their NbN detectors for many years [39]. However, HSQ has several other problems. First, it is incredibly temperamental and difficult to work with. This had the positive effect of causing the development of my current sample cleaning routine, which benefits any resists we use. However, it also means that the yield of HSQ-made devices will likely be low. Additionally, it requires the use of developers that are all problematic.

HSQ will develop if exposed to water, so it is critically important to keep the sample, bottle, and syringe clean. PTFE (Teflon) syringe filters should also be used instead of the standard filters, and these can only be obtained from the supply shop inside the cleanroom at NTW. The other filters can also be purchased downstairs at the main office. A new pair of gloves should be worn when handling the HSQ out of the bottle.

Process:

1) Remove HSQ from refrigerator and let sit to warm up to room temperature in a fume

hood

2) Scribe and blow clean wafers with nitrogen gun

3) Sonicate wafers in acetone for 5 minute (float a dish of acetone in the water in the sonicator)

4) Rinse wafer with isopropanol and blow dry with nitrogen gun

5) Bake wafers for at least 10 minutes at 85 °C on a hot plate to dehydrate

6) Wipe down spin coater and lid with acetone

7) Change gloves

8) Attach PTFE filter to syringe

9) Pour HSQ into syringe and insert plunger

10) Set spinner to: 1000 RPM, 500 RPM/s, 60 s

11) Load sample onto spinner chuck

12) Test centering

13) Drip a few drops (enough to cover sample) of HSQ onto the sample

14) Spin

15) Bake sample for 4 minutes at 85 °C on a hot plate

Then the samples should be inspected. This is the point at which any contaminants on the sample will become obvious, as they will lead to bubbles or other defects in the HSQ. The color of light reflected from the sample is determined by the thickness of the resist, and a color gradient signifies that the resist is not uniform over the sample area.

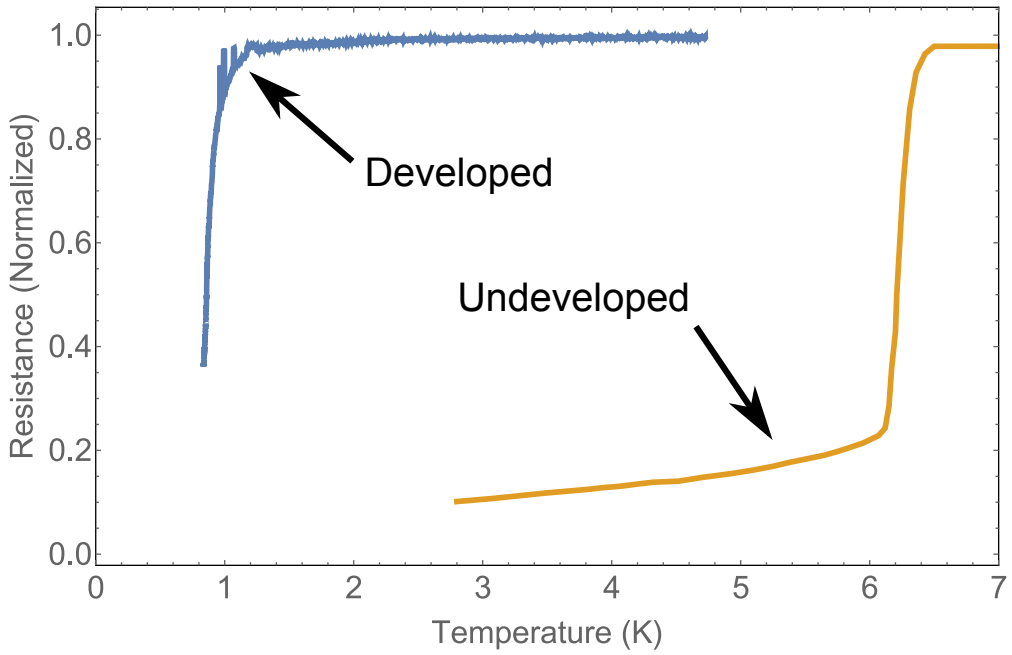

Figure 14: A normalized plot of resistance versus temperature showing the superconducting transition of two similar unpatterned MoSi thin films. One film had been developed using the standard procedure for CD-26, and the other had not.

After writing, I tried three different developers without success. First, I tried CD-26, which is the standard HSQ developer and contains 2.5% TMAH. This developer appeared to work well enough, although it did not have quite as high contrast as we would have liked. However, we discovered later that even this low concentration of TMAH was damaging the MoSi films and causing a large fraction of them to not superconduct at all. Figure 14 shows the difference in superconducting transition temperature between two blank films, one which has been developed with CD-26, and one which has not. The undeveloped film has a transition temperature above 6 K, while the film that was developed for 3 minutes in CD-26 has a transition temperature near 1 K. The second developer we tried was a recipe containing only NaOH and NaCl, which claimed to achieve very high contrast in HSQ [40]. Unfortunately, despite following the recipe and recommendations in this paper, we were never able to achieve anything resembling the pattern we were writing, and ended up with something beyond recognition. The final developer we tried was a 25% TMAH solution, which produced very nice, high contrast lines, but also destroyed our thin films entirely

during the development. The one successful detector I made used CD-26, and we just got lucky that one of the films survived the development process enough to superconduct and detect photons.

2.4.3 PMMA with high temperature bake

Summer 2019, I did and REU at NIST Boulder, and while I was there I spoke with Dileep Reddy, a postdoc in Sae Woo Nam's group. We had decided to switch to PMMA at that point, so I took notes on his recipe for writing detectors with PMMA, and this is what our current process is based on.

The main difference from the previous procedure is the temperature of the bake. NIST does not worry about possible crystallization of the MoSi due to high heat, and they heat their devices up to 180 °C during the coating process. I have adopted this strategy, although it needs to be adjusted for the hot plates at NTW, which are not uniform spatially or temporally. Either the set point must be a temperature several degrees above the desired temperature, or heat probes must be used to ensure that the sample is reaching the proper temperature. The sample itself must get above 160 °C for PMMA to properly adhere, which may mean a hot plate temperature of 190 °C or more.

The other major difference at NIST is the use of Electra92 as a charge mitigator. This conductive resist is spun on top of the PMMA to a thickness of about 100 nm and supposedly prevents charge buildup during electron beam writing. However, no noticeable difference in the quality of our patterns exists between samples that used Electra92 and those that did not.

2.4.4 Current spin coating process

Cleanliness of the samples is critical for ensuring successful detectors, so after scribing the wafers with a diamond tip scribe in the cleanroom, they are blown with compressed nitrogen and then sonicated in acetone for five minutes. After sonicating, the samples are rinsed in

isopropanol to remove residue from the acetone, then blown dry and baked. The samples must be at least 160 °C for one minute, but because the hot plates are not reliable or uniform a 200 °C bake for three minutes is used. Without this bake, the PMMA will not adhere to the sample, resulting in the lines of the detectors falling over or shifting from their desired positions (see Fig. 13). After baking, the samples are blown dry again.

A spin coater is used to cover the samples with a uniform layer of resist. Spin coaters spin a sample very quickly to create a uniform, thin layer of resist, on the order of 100 nm. Once again, it is crucial that the samples are clean and free of particles before spinning, as any tiny particles will imprint themselves on the spun resist and cause an uneven coating.

In our current process, PMMA is spun on to the samples. The NIST group uses a special 3% PMMA mixture, but we approximate the thicknesses they achieve by using a 4% PMMA solution and spinning at a high RPM. The settings for the spin coater are 4000 RPM for 90 s, with an acceleration of 500 RPM/s. After spinning, the samples are baked again the same way (200 °C for 3 minutes).

2.5 Electron beam lithography

Electron beam lithography (EBL) technology evolved out of scanning electron microscopy, and many electron beams today are still converted scanning electron microscopes. The basic function of EBL is to form a very tight beam of electrons by focusing the beam with magnetic lenses. It then rasters the beam across a target, exposing regions of the target to high voltage electrons.

2.5.1 Pattern Design

For SNSPDs, I based my patterns off of [15], which gives a nanowire width of 130 nm and a pitch (center to center spacing) of 215 nm and a rectangular active area. Although my patterns use a circular active area and have specially rounded corners, the widths and pitch of the lines remain the same. The patterns are a single-nanowire design, and are designed

for use with a standard single-mode fiber, which has a core diameter of 6-8 um. To cover this, the active area of my detectors is a circle with a diameter of 15 um.

Originally, the patterns were made in L-Edit, which you can get a license for by asking the NTW staff. Then, the patterns were fractured in CATS into polygons that the ebeam can read. However, I have since shifted to designing the files algorithmically using Python libraries and exporting the files in GDS format. This can then be read in to BEAMER, an expensive commercial EBL file preparation program that NTW currently has a trial license for. BEAMER can do many useful things including secondary electron correction, but I simply use it to fracture the files, and the crop them for writing dose arrays. My code for designing the patterns is available on GitHub [41].

A longstanding problem when writing patterns using electron beam lithography is known as the proximity effect [42]. This effect is caused by electrons scattering as they pass through the electron beam resist, resulting in secondary exposure of nearby regions of the resist. A profile of one example of the proximity effect is shown in Fig. 15. The end result of this effect for the SNSPD designs we write is that, without correcting for it, the lines at the center of a detector will be more exposed than the lines at the edges, and therefore thicker. This is because the lines at the center have secondary electrons from all sides, while the lines at the edges only have half the amount of secondary electrons. There are several ways to compensate for this [43], including with complicated software such as BEAMER that adjusts the beam parameters at each location in order to perform proximity effect correction (PEC). However, the route that I have taken is the simplest solution, which is to make the secondary electron dose the same for all points on the detector. This is accomplished by extending the pattern of the interior of the detector outside, so that it is surrounded by a large region of lines that give the same proximity effect. An example of this in practice is shown in Fig. 16. The lines extend out from the detector at least 20 microns in all directions.

Another concern with electron beam lithography is simply the amount of time it takes to write a pattern. For SNSPDs like in Fig. 16, we use a beam that is about 10 nm across

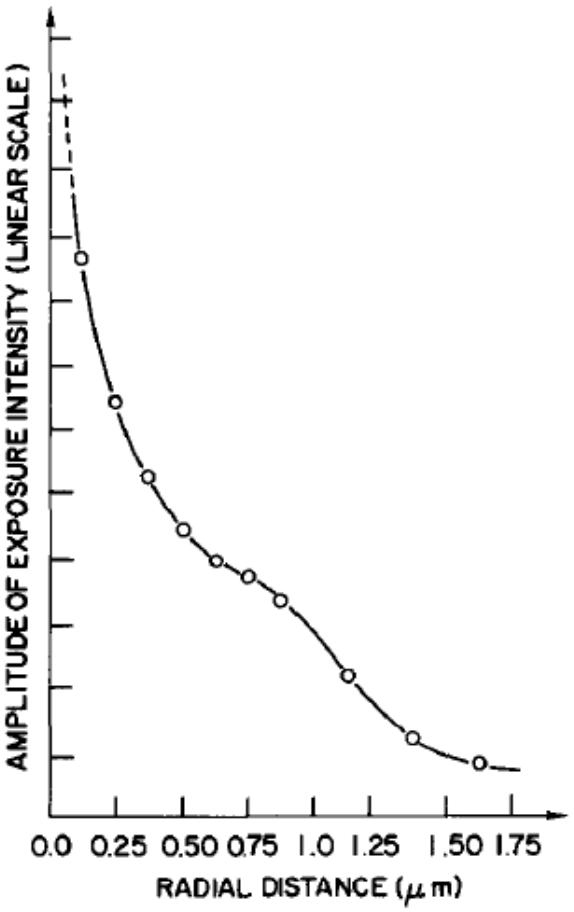

FIG. 6. Exposure intensity distribution obtained experimentally using a 25-kV 0.2-μm-diam incident beam on a silicon substrate with a 6000-Å PMMA resist developed in MIBK:isopropyl alcohol (1:1) for 60 sec. The exposure intensity distribution approximates the sum of two Gaussian distributions: $C_1 \exp(-r^2/B_1^2)$ for primary electrons and $C_2 \exp(-r^2/B_2^2)$ for BS electrons. For best fit, $B_1 = 0.1$–0.2 μm; $B_2 = 1$–1.2 μm, and $C_1/C_2 = 1.5$–3.

Figure 15: The exposure of an electron beam resist as a function of the distance from the point being written, from [42].

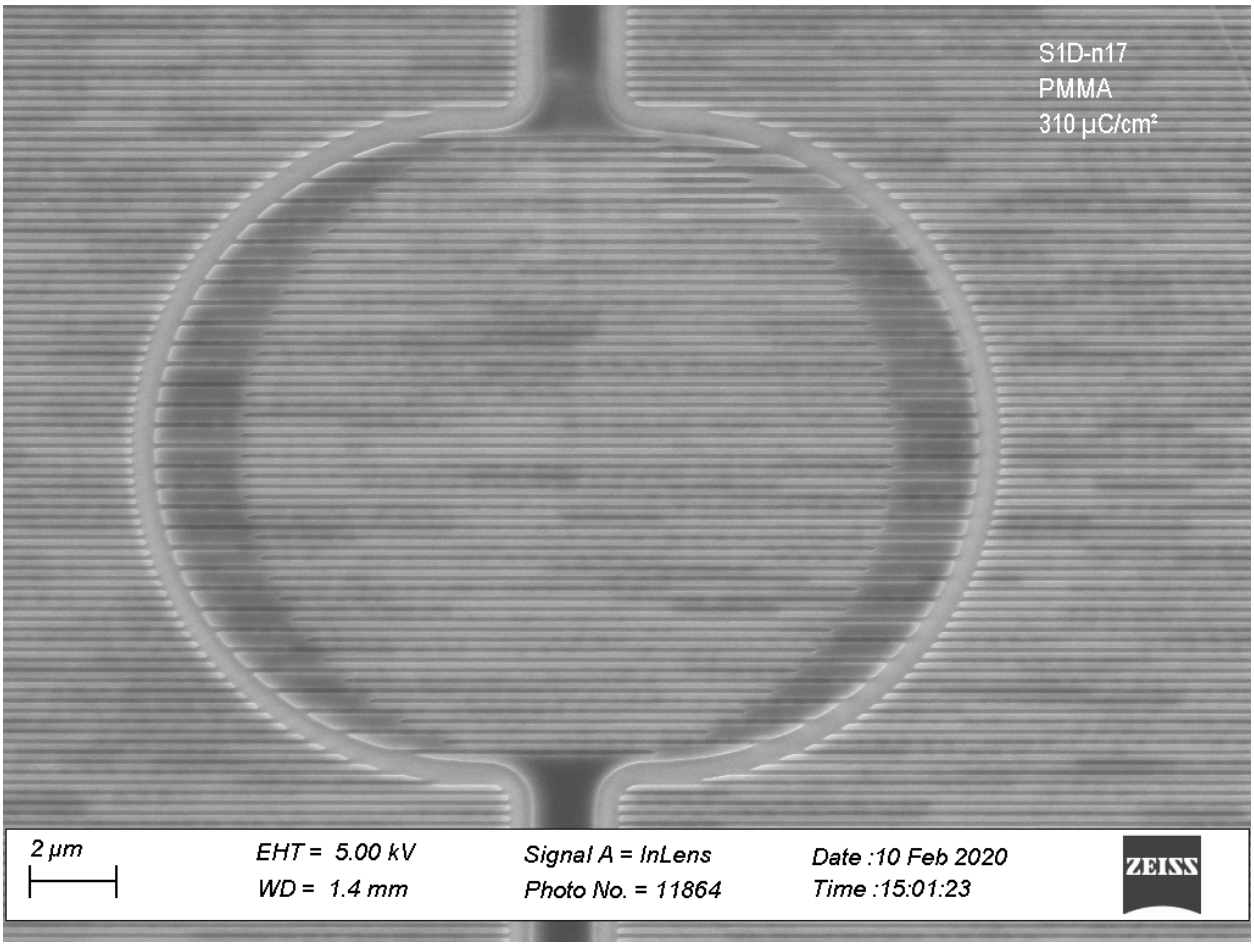

Figure 16: A scanning electron migrograph of the most recent iteration of our SNSPD pattern, written in PMMA.

and delivers 1 nA of current. For the relatively small area (about 50 microns square) of the active area and proximity effect correction lines of an SNSPD, this is not a big issue. But for the larger parts of the pattern that form the wires to the gold electrical contacts, writing those large ares could take hours. So instead, we break the pattern into two pieces: one written with the 1 nA beam, and one written with a 100 nA beam that is about 100 nm across. Because of changes in alignment that can happen during writes, the two patterns should be overlapped by a few microns to ensure continuity where they meet. Each of the patterns will need to be written at a slightly different dose, so separate dose arrays must be done for each. For the bridge style detectors, currently only the large beam is used, but this leads to artifacts from the way the files are stored and so it is desirable to switch to the two-exposure model in the future. These artifacts can be seen in Fig. 17b.

Finally, care must also be taken to limit current pinching at turns in the wire, where sharp corners can cause the local current density to exceed that of a straight wire and cause the device to go normal. Fortunately, Clem and Berggren derived analytic equations describing the optimal geometry for various types of turns in superconducting wires [44]. For a tight 180 degree turn, the shape of the inside of the turn should be

$$y_{opt}(x) = \pm\frac{2W}{\pi}\cos^{-1}\left[\exp\left(\frac{\pi x}{2W}\right)\right], \tag{3}$$

where W is the width of the wire, and twice the width of the gap between the wires. This is not our exact geometry, but using this formula with our wire spacing will give a nearly-optimal turn. It is possible that, with further effort, one could find a truly optimal solution for our geometry.

2.5.2 Loading and alignment

The files are designed so that the patterns for all four of the films on the sample are in one file, with the appropriate spacing. In the EBL terminal, only the location of the pattern can

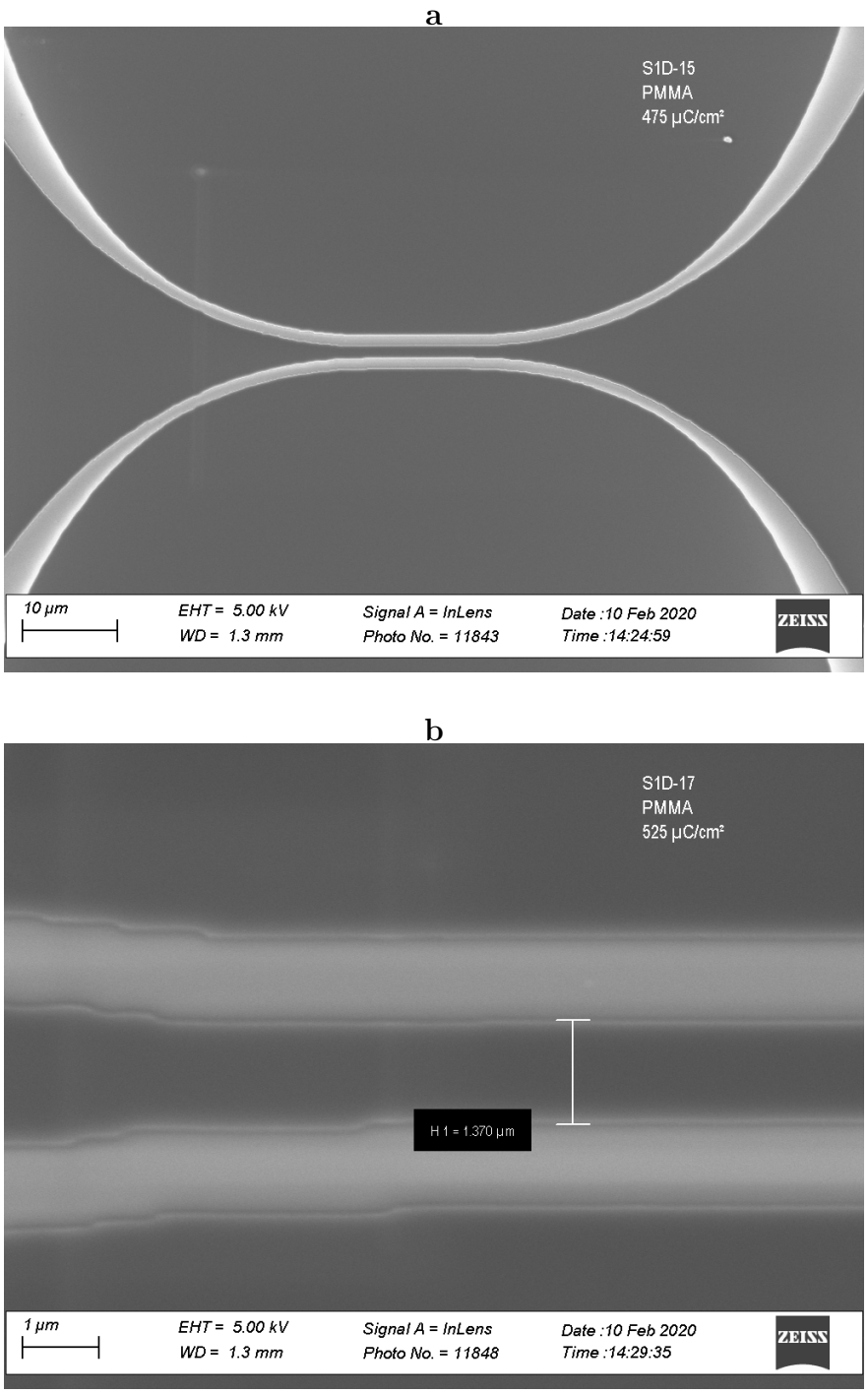

Figure 17: A scanning electron migrograph of a bridge detector written in PMMA: (a) a wide view of the active area of the detector; (b) a close up of the same detector showing the digitization of the curves and the width of the wire.

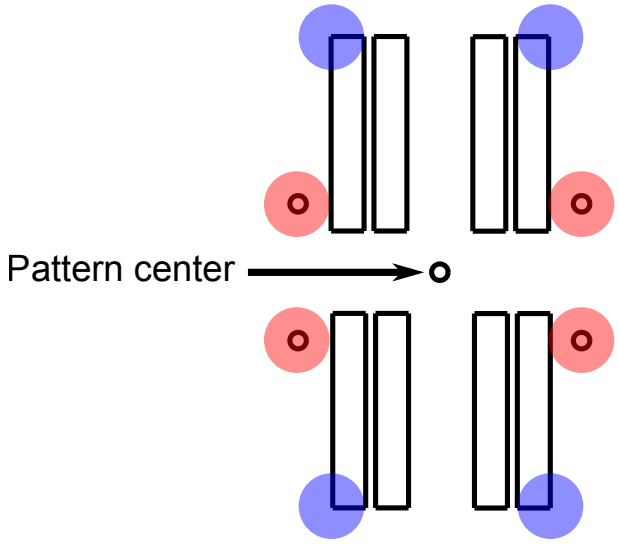

Figure 18: A schematic of the electrical contacts for our devices. To locate the center of the pattern, which the EBL needs, either average the positions of the four corners (blue) or the four alignment dots (red).

be specified, and not the orientation, so the orientation must be manually corrected during the alignment process. Then, it is important to obtain a very accurate position for the center of the sample, from which all four of the patterns' locations are determined.

First, the samples are loaded into the holder for the electron beam lithography machine in Bay 1 of NTW. We typically used Holder 5. We developed a special alignment procedure to be able to align the samples without any special markers on the wafers. The gold contacts are 300 µm apart, and a set of four detectors are written at once. In the optical microscope station, after ensuring that the samples are within the height limits, they must be oriented precisely parallel to the holder. There is an adjustment screw in the holder that can rotate the samples. To check the rotation, zoom in to one of the gold pads. Then, use only one of the knobs on the microscope to translate along one axis. For example, in Fig. 18, align the microscope crosshairs to the top left corner labeled in blue, and then translate down to the bottom left corner labeled in blue. The crosshairs of the microscope should remain on the edge of the pad, all the way to the corresponding pad on the other side of the sample. Adjust until the rotation offset from one side of the sample to the other produces

an error of only a few microns. Once they are aligned rotationally, take measurements of the outermost corners of the four outermost gold contacts, shown in blue in Fig. 18, and the average of these four points is taken to be the center of the write (marked with the arrow). Alternatively, the mask has five alignment dots drilled into it that can be used the same way, marked in red in Fig. 18. However, these dots do not always show up, or appear only as crescents on some samples. Either way, write down the four (x, y) coordinates and calculate the center.

Then, after loading, these corner measurements are corrected using the EBL's SEM function. The reason to measure the corners instead of using the SEM to directly locate the desired positions of the detectors is that the SEM function will expose any PMMA in the picture, overwriting the detector patterns. Additionally, the optical microscope alignment is generally accurate only to within a few hundred microns, which is not accurate enough to reliably place detectors in the 300 µm gap between the contacts, so the four corner measurements must be corrected in the SEM. Direct the SEM to navigate to the positions obtained with the optical microscope, and then adjust the location to center the pattern on the SEM display. Once the four corner measurements are updated with the SEM values, the center of the pattern is set to the average of those four measurements, like with the optical microscope.

2.5.3 Writing

The patterns are written with varying doses determined from writing dose arrays and observing them in the SEM. For nanowire detectors, two different doses and beams are used: a large 100 nm, 100 nA beam for the coarse features like wide wires to the contacts, and a small 10 nm, 1 nA beam for the fine features. Follow the instructions in the EBL standard operating procedure binder.

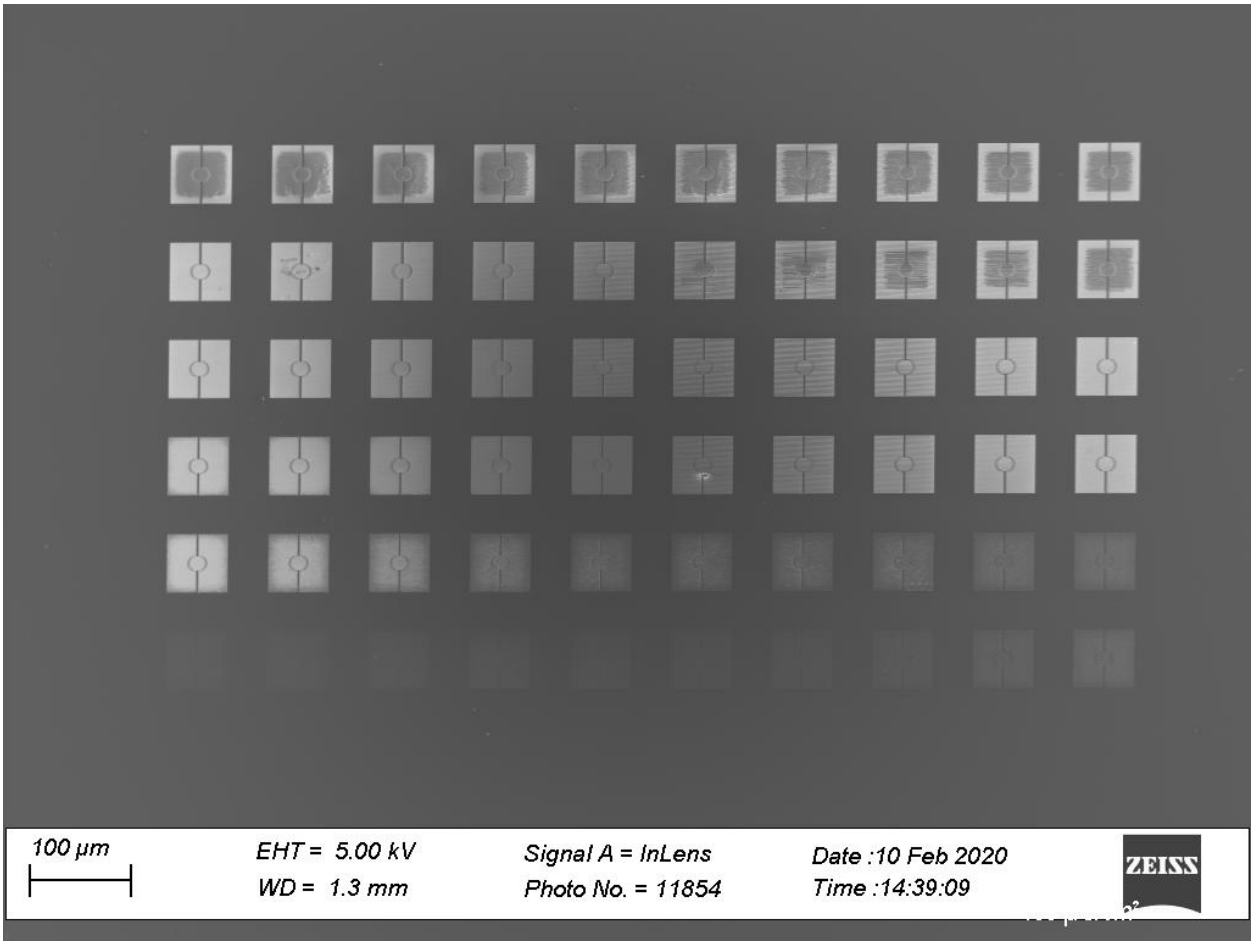

Figure 19: A scanning electron micrograph of a dose array in PMMA resist on SiO_2. Dose arrays on the EBL system at NTW snake back and forth. Here, the lowest dose is in the bottom left. The dose increases then from left to right, but then the next higher dose is the rightmost pattern on the second row from the bottom, with doses increasing right to left in that row, and so on.

2.5.4 Dose arrays

Every different design file, resist, and substrate will need to be written at a different dose or exposure. Doses are measured in $\mu C/cm^2$. Writing dose arrays can determine the correct dose for a given pattern. A dose array is simply an array of a portion of a pattern where each element is written at a successively higher dose. For our recipe of PMMA, common doses are a few hundred $\mu C/cm^2$, so one might write a dose array going from $100\,\mu C/cm^2$ to $600\,\mu C/cm^2$ in steps of $25\,\mu C/cm^2$. Then, once developed, the different doses can be compared in the SEM to find the dose that has the best balance between underexposing and overexposing the pattern. An example of a dose array written in PMMA is shown in Fig. 19.

2.6 Development

After writing, the PMMA is developed using the standard procedure: 3 minutes in a 3:1 IPA:MIBK solution, with gentle agitation every 30 seconds. To avoid breaking the samples when removing them from the container, it is best to use one of the plastic baskets available in the NTW cleanroom to lower the sample into the developing solution so they can be easily removed after three minutes. Then the samples are rinsed with water and blown dry.

2.7 Scanning electron microscopy

The only way to effectively characterize the developed resist structures before etching is to use a scanning electron microscope (SEM). Unfortunately, observing PMMA samples in the SEM requires destroying the samples. Since PMMA is both insulating and a positive tone resist, it renders most of the sample non-conductive. If the sample is observed in the SEM in this state, electrons will build up in the PMMA and this electric charge will cause future electrons' trajectories to distort, leading to a blurry unusable image. In order to address this, the samples must be coated in a thin layer of a conductive material, in this case gold. There is a small sputtering system in the Biohybrid Lab at NTW that is used for this purpose.

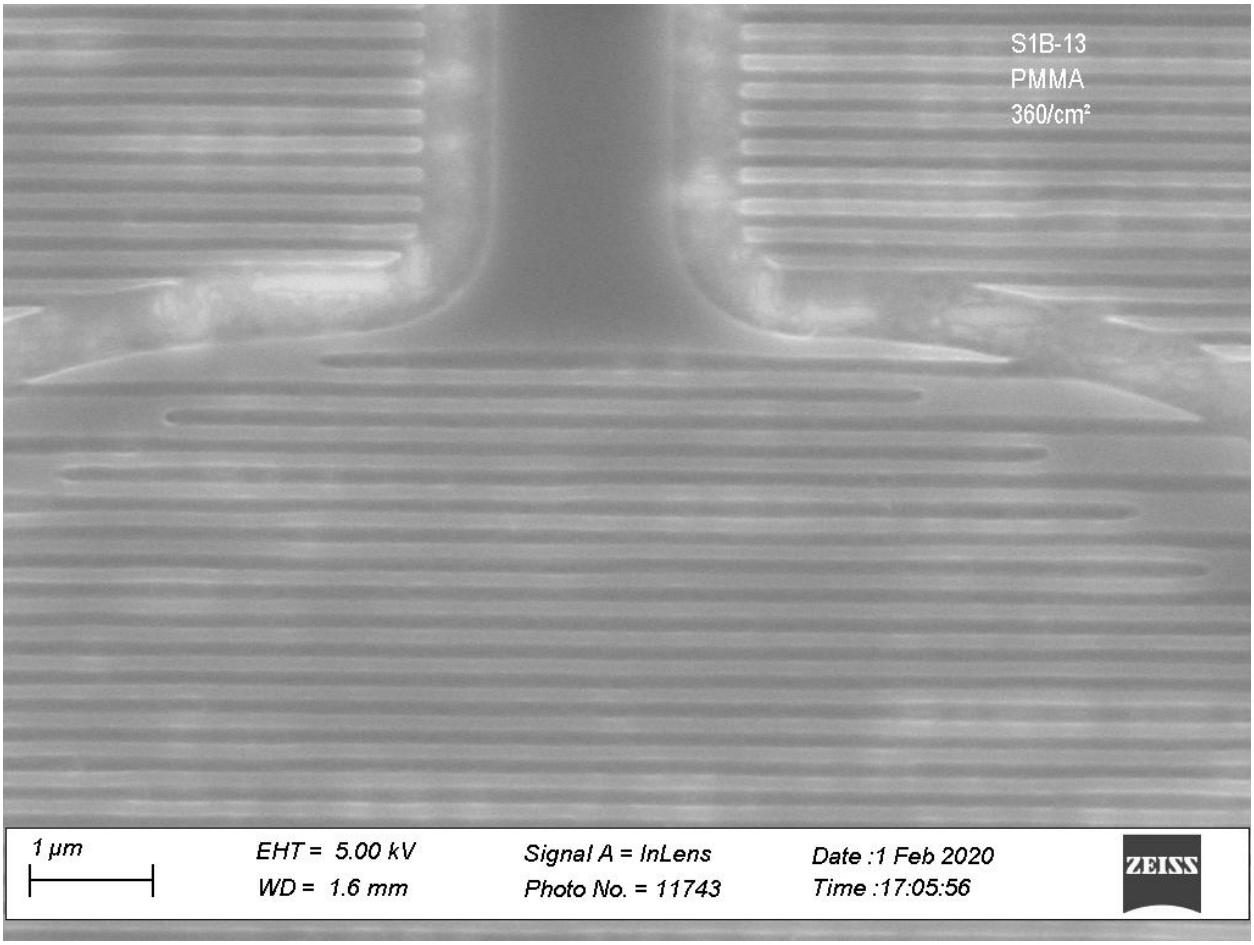

Figure 20: A scanning electron micrograph of under-exposed PMMA resist on SiO_2. Because PMMA is a positive-tone resist, under-exposure leads to the resist between the lines not being fully removed during development, as can be seen here by the splotchy and low-contrast regions outside the nanowire.

Following the standard sputtering procedure will put a few nanometers of gold on the sample, which is plenty to keep it from charging. Then, the samples can be put in the SEM like normal. Because this destroys the sample, samples which will be processed further should be made alongside an identical sample that will be used in the SEM for characterization.

There are a few key observations to make with the SEM. First is simply to observe that the pattern wrote correctly and that there are no gaps or holes, and that the alignment is acceptable. This can be caused by both too high exposure and too low exposure. In positive tone resists like PMMA, over-exposure will cause lines to become too narrow and collapse, as seen in Fig. 21. Second is the see if the resist is cleared between the wires of

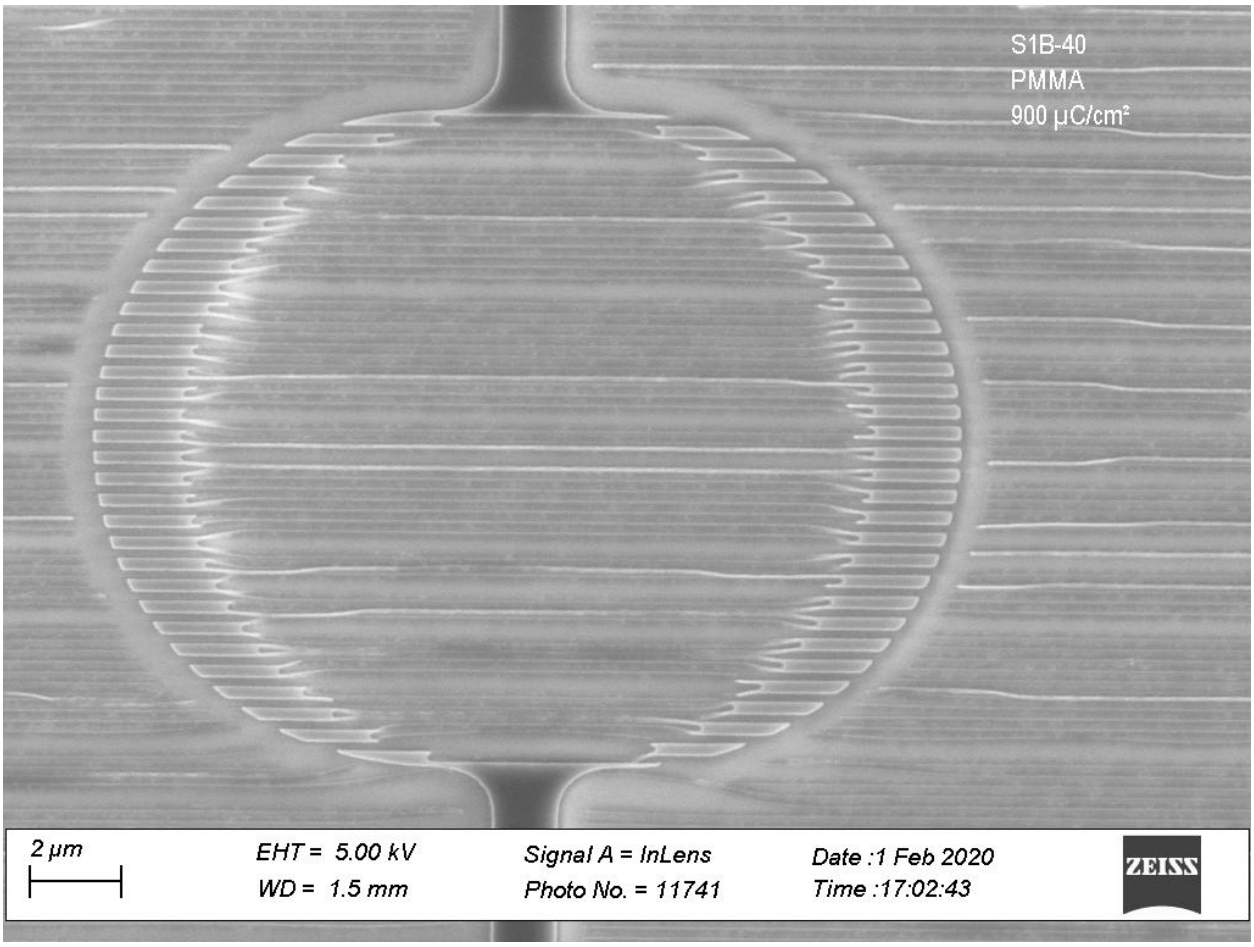

Figure 21: A scanning electron micrograph of over-exposed PMMA resist on SiO_2. Because PMMA is a positive-tone resist, over-exposure causes the lines or resist to become too narrow and collapse.

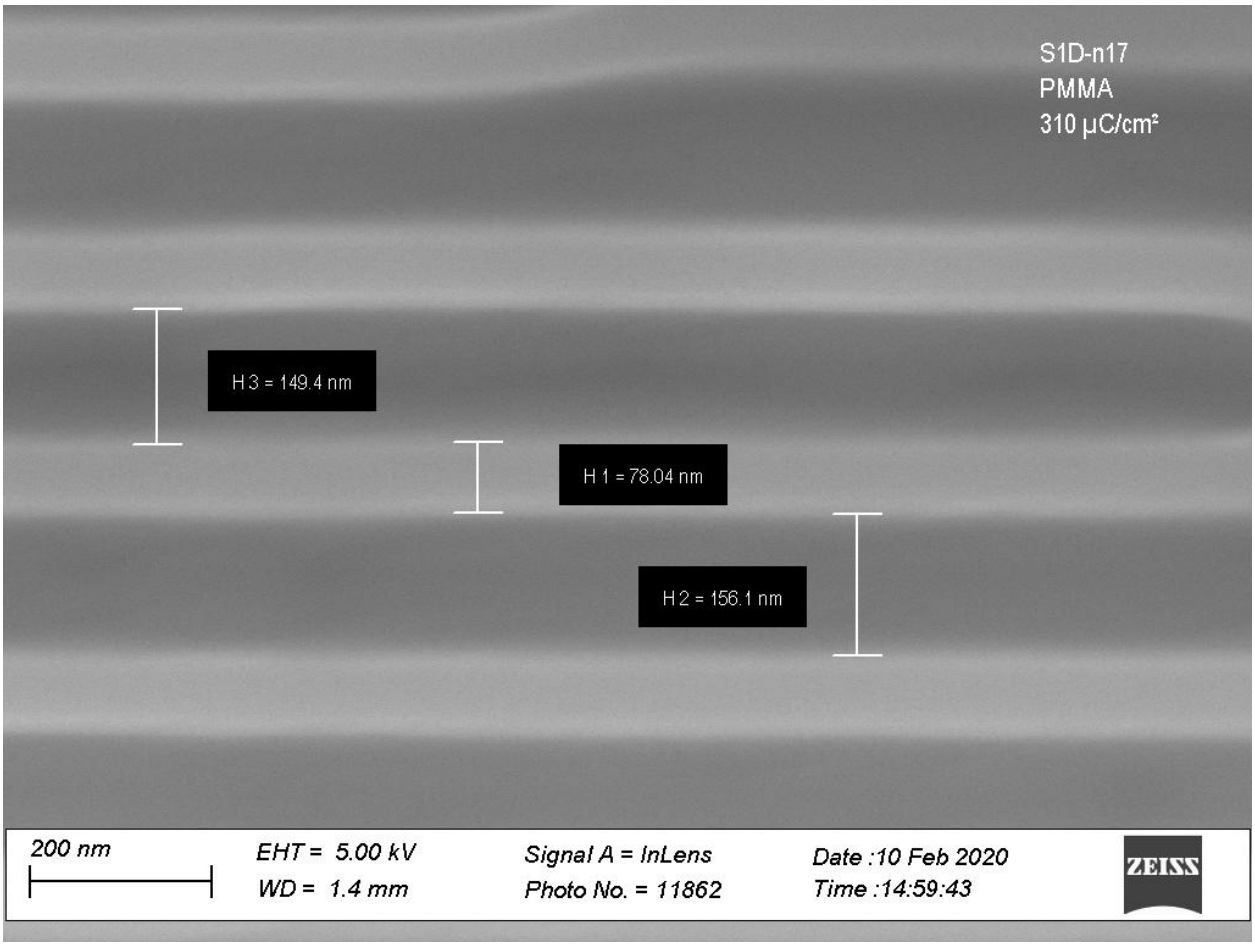

Figure 22: A scanning electron micrograph of linewidth measurements of PMMA resist on SiO_2.

an SNSPD. It is often the case that the resist will show the pattern that was written, but there will still be some resist between the lines. This can be checked by noticing the reduced contrast between the lines and spaces in the image, like in Fig. 20, and comparing it to the contrast where there are larger areas that have definitely cleared. Finally, it is useful to make precise measurements of the thicknesses of the lines, to see if they have grown or shrunk during the write, as shown in Fig. 22. To correct for this, it may be possible to adjust the dose, but more than likely it will require adjusting the pattern file to compensate. In the example of Fig. 22, the lines are too narrow, so the lines in the pattern file must be widened to achieve the desired line widths.

2.8 Reactive ion etch

The last nanofabrication step is the etch the superconductor. We have found that reactive ion etch (RIE) produces the best results, after also trying the ion mill in Lab18. To use the RIE system in NSL, the samples must be mounted on a standard 4 inch wafer. This can be accomplished with very small pieces of double-sided carbon tape, which can be removed later with acetone.

Although the amount of time needed to etch a certain thickness of superconductor should remain somewhat constant, RIE systems are known to drift with time. To work around this, once a rough etch time has been determined, a sample should be etched for about 75% of that time, and then a series of short etches should be used to finish the job. To determine if an etch is finished, measure the resistance across the gold contacts of each of the four films on a sample after each etching step. As the films get gradually etched from a broad film into a narrow nanowire, the resistance will increase dramatically and then plateau once all of the exposed superconductor has been etched, as shown in Fig. 23. In this case, the etch should be stopped at around 80 s. Be careful with the multimeter around thin films. Always start measuring on the MΩ scale and slowly increase the precision until you can measure the resistance. Connecting a multimeter set to measure in kΩ to a nanowire

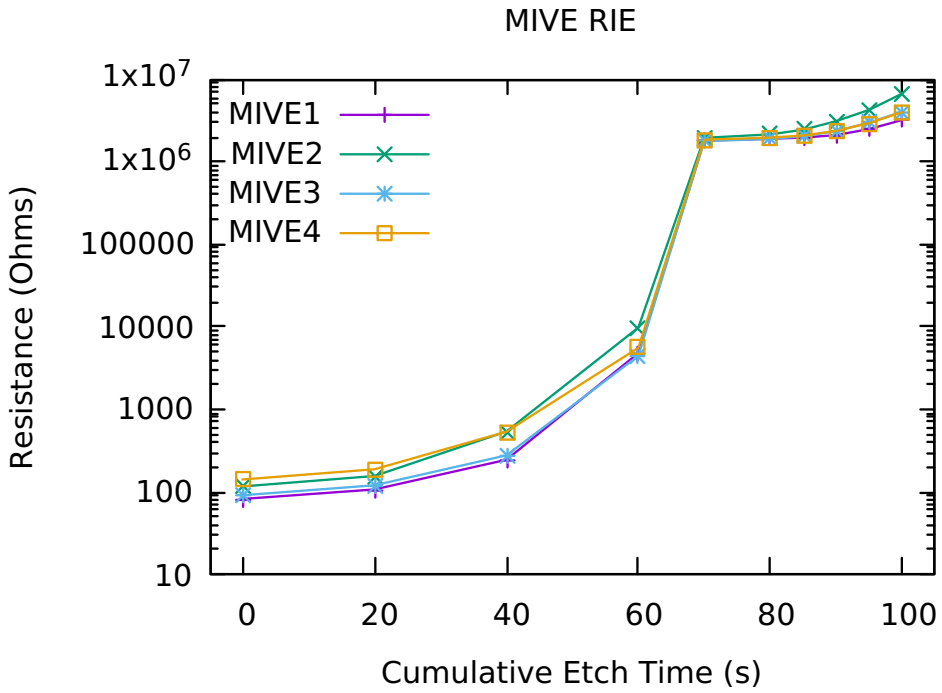

Figure 23: The resistance of four samples of MoSi films as they are etched into a nanowire by reactive ion etch.

will put too much current through the device and possibly destroy the nanowire.

The recipe we currently use for RIE etching is saved on the machine as "`KD_CF4_etch`." The parameters are also shown in Table 1. The machine is very easy to use, and I typically run it in fully automatic mode. Just be sure to adjust the etch time in the file before starting.

If the detectors were written with HSQ, the sample is now in its final state. HSQ does not need to be removed because exposed and developed HSQ is effectively just glass (SiO_2) and can serve as a protective layer above the nanowire. It is also nearly impossible to remove without damaging the nanowire. If the detectors were written in PMMA, however, simply remove the PMMA using acetone. This will leave the nanowires exposed, so it may be best to apply a protective coating of some sort afterwards, such as SiO_2. This could be done using Lab18, although a new mask would be needed to cover the electrical contacts.

Parameter	Value
Pressure	30 mTorr
ICP	0
RIE RF power	50 W ± 10 W
Temperature	25 °C
RF stable time	1 s
CF4 valve setpoint	50%
He pressure	2 mTorr
All others	0

Table 1: RIE settings for etching with CF_4.

2.9 Wire bonding

After etching, the detectors need to be electrically connected to the rest of the circuit. The most straightforward way is to wire bond the sample to a printed circuit board (PCB) and then connect the PCB to a SMA coaxial jack, which can be connected to the cables in the cryostat.

First, mount the sample onto or next to the PCB using either cryogenic varnish or nail polish. Wait for the adhesive to dry (24 hours or more for nail polish). If the PCB is soldered onto some other container, be sure to use low-temperature solder, as regular solder superconducts and will not conduct heat effectively away from the detectors.

Then, have the sample wire bonded [45]. We have a wire bonder in room 4115, or Peter Janney at NTW can do it for you. If possible, make two or more bonds for each connection, because wire bonds break easily and can sometimes break spontaneously when cooled in the cryostat. Beware the ball bonder [46], which is next to the wire bonder at NTW. It is far easier to use, but the electrostatic discharges it uses can potentially destroy the thin films and nanowires. For bulk film samples it is probably okay, but for nanowires it will likely destroy the film and cause the resistance to change drastically. Continue monitoring the resistance even after the RIE is finished to notice if a certain step is changing the resistance of the devices, which is a sign of damage to the superconductor.

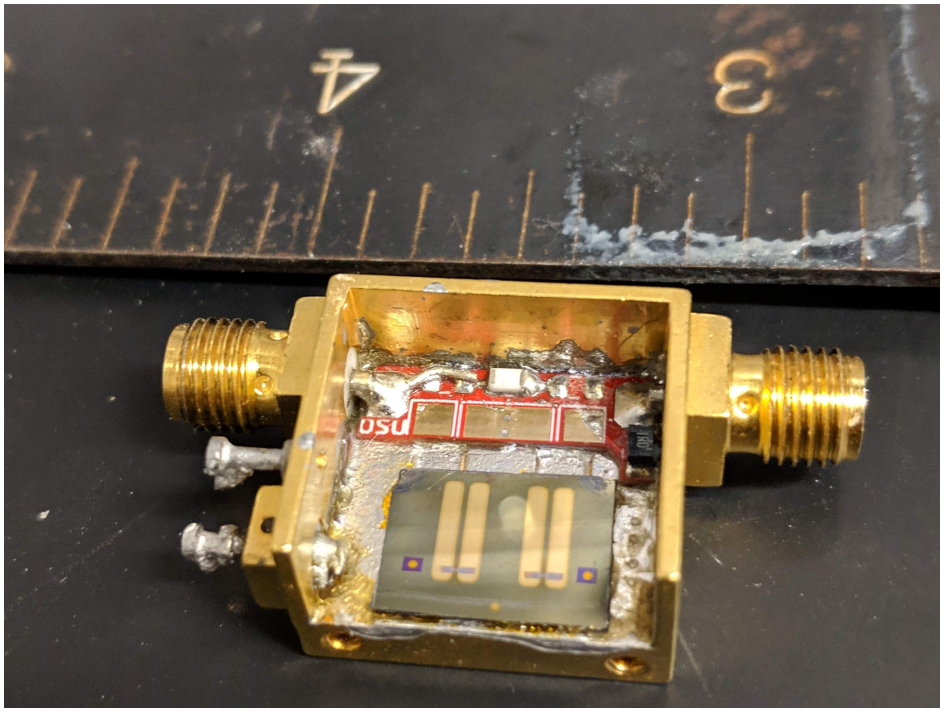

Figure 24: A sample containing two SNSPDs mounted in a modified amplifier box, ready to be wire bonded. The ruler is in inches.

2.10 Packaging

Because we are not building an optical cavity around our detectors and coupling them to a fiber directly, the packaging can be much simpler than commercial detectors. My current favorite is to take amplifier boxes and strip out the PCB, replacing it with a custom board that the detector is wire bonded to. This is shown in Fig. 24, with the detectors mounted and ready to be wire bonded. The metal lid of the box has holes aligned with the positions of the detectors to feed a fiber into, suspending it a few cm above the detectors. The box can be screwed into the cryostat, and it already has SMA connections.

2.11 Future directions

Now that the capabilities have been built up, the next steps are to begin making exciting devices like bridge detectors. Although the existing pattern (Fig. 17a) is likely sufficient for a first attempt, the coarse resolution of the pattern file leads to artifacts on the edges of the

device (Fig. 17b). To counteract this, a new design should have separate files for the narrow part of the device and the larger electrical leads to the device, with the narrow sections written at higher resolution to avoid these artifacts, like is done currently for SNSPDs.

In [29], Vodolazov gives predictions for the initial electrical response that comes from the detection of a photon. These predicted responses may show signs of the photon's energy or the number of photons detected that can be measured after amplification. So far, no superconducting single-photon detectors can measure the energy of a detected photon, but if the exact timing was known their model suggests that the delay between incidence and detection could give some information about the energy. Measuring this effect is one potential experiment that could be performed to learn more about this detection mechanism. Others include measuring the detection's response to magnetic fields, which will influence the vortex formation and motion as well as the depairing and switching currents.

It will also be important to characterize how the geometry affects the device's performance, if these devices are to be used in other applications like on-fiber detectors. Experimental results of how the width, thickness, and uniformity affect the detection efficiency may help guide the design strategy for future applications of these devices.

3 On-fiber detectors

One of the key difficulties when fabricating single-photon detectors is how to couple the light from a fiber into the detector. In this section I will describe my efforts to integrate single-photon detectors directly onto optical fibers. This could eliminate many of the difficulties encountered when designing traditional single-photon detectors.

Beyond the standard optical stack used in most current devices, two major strategies have been used for coupling the to the detector, in addition to the standard optical cavity stack. The first is to couple the light into a waveguide, and have the SNSPD embedded in that waveguide. Attempts to do so have had limited success coupling from the circular mode

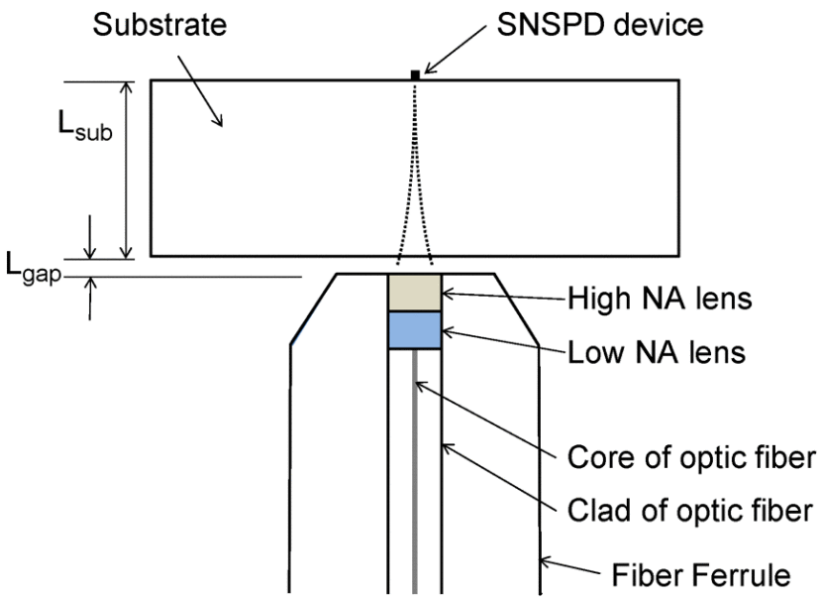

Figure 25: A schematic of one approach to coupling light into an SNSPD integrated into a waveguide from a fiber, from [48].

of the fiber into the rectangular shape of the waveguides. Detection efficiencies using these methods have reached up to 75% [47][48]. It is likely physically possible to achieve higher efficiencies through more adiabatic couplings, but this would be very difficult to fabricate in practice.

The second strategy is to write a SNSPD on the end of the fiber itself, as shown in Fig. 26. The authors of this study claim that the coupling efficiency is high, although they incorrectly assume that the efficiency can be calculated by the overlap of the mode with the geometry of the detector [17]. This assumes that all field inside the nanwire is absorbed, which is not the case. Additionally, due to Gallium ion poisioning from using a focused ion beam to make the devices [49], the system detection efficiency is even lower, less than 0.01%.

However, our approach is to write single-photon detectors on the side of a fiber. For this, it is important to look at the side-polished fibers that the detectors will be written on. Side polished fibers have been around for several decades now [50], and are used in many experiments as part of sensors. In these experiments, the fibers are submerged in a liquid or gas to be studied, and the interaction between the evanescent field of the light in the fiber

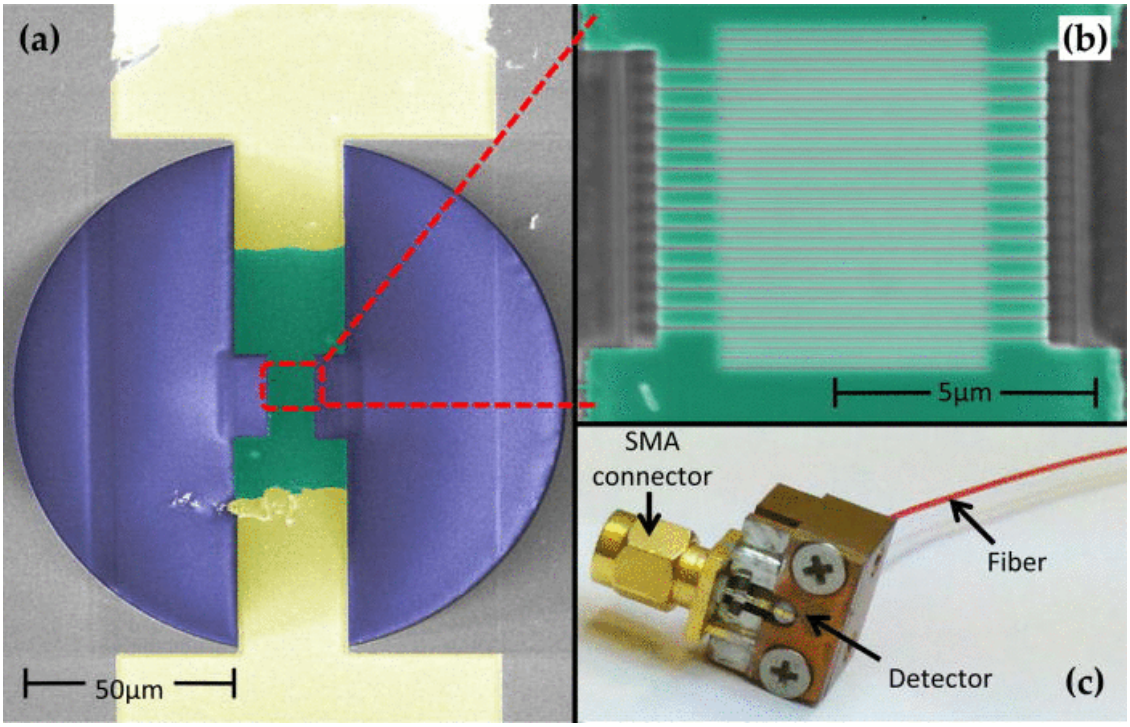

Figure 26: An SNSPD written directly onto the end of an optical fiber, from [17]: (a) and (b) show the end of a fiber, with the SNSPD centered over the core of the fiber; (c) shows the assembled package.

and the medium being studied can be used to measure properties of the medium. In one experiment, side polished fibers were used to measure the concentration of gaseous ammonia present at the surface of the fiber [51].

The experiment most similar to this work was conducted by Sherwood *et al.* in 2005 [52]. In their work, they polished a fiber themselves to expose the evanescent field, and used two-photon polymerization to construct a ring resonator on top of the fiber, which coupled to the core of the fiber. This ring resonator was then used as a sensor to measure various properties of the environment. However, this was not used as a photon detector, and the fabrication process was far less precise due to the relatively large dimensions of the structure being fabricated.

3.1 Side-polished fibers

This direction of exploration looks for new ways of coupling light to the detector, instead of exploring different detection mechanisms. The electromagnetic field of a fiber, although primarily confined to the core, does extend outwards into the classically forbidden region in the form of an exponentially decaying evanescent field. By reducing the size of the cladding, or eliminating it altogether, it is possible to couple a detector to the evanescent field of a fiber. This could avoid the difficulties of coupling from a fiber to a waver-based detector, and the need for an optical cavity to cause the light to pass through the detectors many times. The coupling and optical cavity have been one of the main focuses of SNSPD research for the past decade, and an on-fiber detector may be able to avoid the challenges of both.

Side polished fibers are standard optical fibers where the cladding has been manually polished down to within a few microns of the fiber's core, exposing the evanescent field (Fig. 27). These fibers are now available commercially [53]. I have made measurements of the fibers' roughness in an AFM, and although they are certaintly much rougher than our silicon wafers, they appear to be smooth enough locally that they might be suitable for detectors. Figure 28 shows a 100 nm by 100 nm region of the fiber, where the height varies

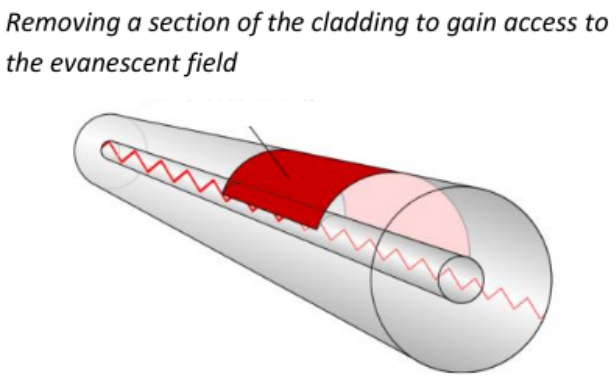

Figure 27: A schematic of a side polished fiber, showing the portion of the cladding that is removed, from [53].

by less than 2 nm.

3.1.1 Simulations

Using the free Finite Difference Time Domain (FDTD) electromagnetic simulation software MEEP [54], I simulated several different geometries of on-fiber single-photon detectors in order to estimate the efficiencies of the different designs. Then, when a real detector is fabricated, it can be compared to these benchmarks.

When simulating a geometry that is closest to the actual device that will be constructed, some approximations had to be made. Because of the large disparity in the dimensions of the key objects, some objects had to be simulated as larger than they actually were, and there properties were changed to compensate. Specifically, the cladding of a fiber is 125 µm across, and the core is 8 µm, but the superconducting thin film is only 8 nm thick. To avoid having an intractably large simulation size, I increased the thickness of the superconducting films, and decreased their absorption by the same factor to compensate. Additionally, I compensated their index of refraction accordingly. My code is available on GitHub [55].

For the side polished fiber simulations, the simulated fiber had a cladding 100 um thick and a core 8 µm thick. There was 1 µm of cladding between the core and the polished

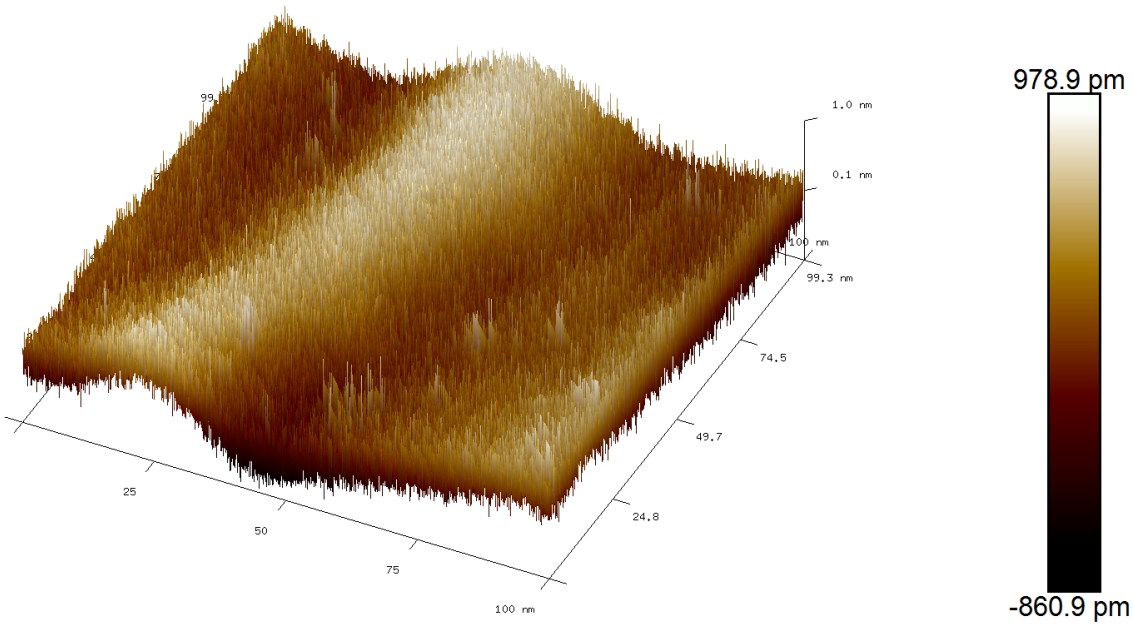

Figure 28: An atomic force micrograph of the surface of a side polished fiber, showing the features of a 100 nm by 100 nm region. Height is not to scale.

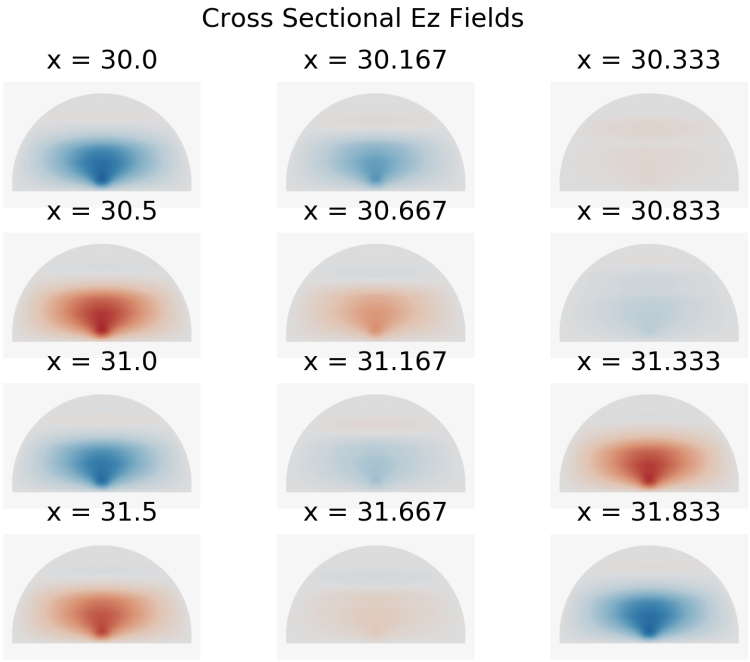

Figure 29: Simulated $\hat{z}$ component of the electromagnetic field's cross sections at different points along the fiber. Units of x are microns.

surface of the fiber. The superconductor was simulated as a bridge-type detector, 2 µm wide and parallel to the core. The superconductor was simulated as 0.5 µm thick, and its absorption was decreased by a factor of 50 to compensate (approximating a 10 nm thick film). The simulation volume was 120 µm by 110 µm by 70 µm, and the resolution was 0.167 µm. The simulation estimated a $1/e$ absorption distance of 2.7 mm, so a detector of more than a centimeter in length would be needed for high absorption. The cross sections of the electromagnetic field from this simulation are shown in Fig. 29.

3.2 Tapered fibers

Tapered fibers are fiber that have been heated up by a flame to become ductile, and are then carefully stretched so that a segment of the fiber becomes very narrow. Fibers can be tapered down to 1 µm or less, and therefore have a very strong evanescent field outside the fiber [57]. A drawing of a tapered fiber is shown in Fig. 30 [56]. In fibers tapered down to

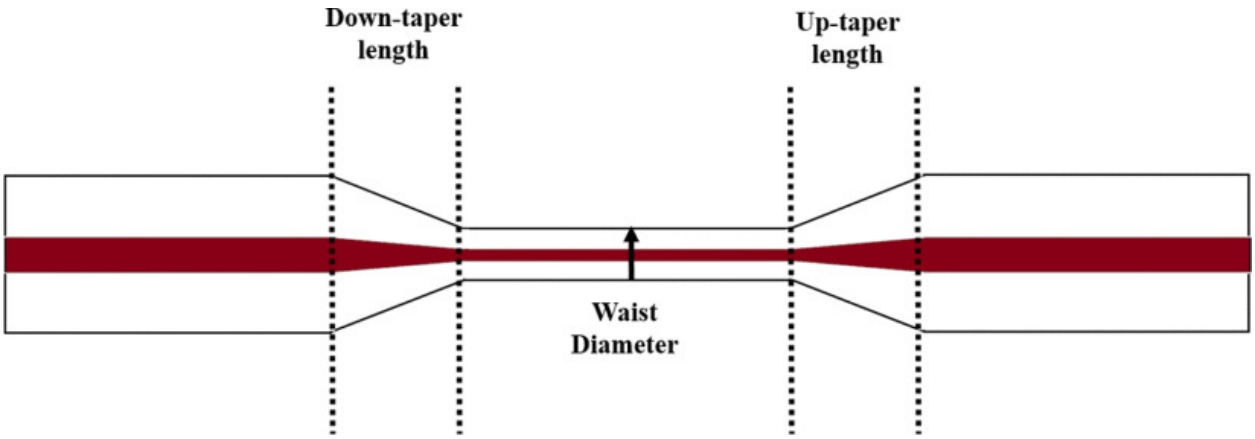

Figure 30: Depiction of a cross section of a tapered fiber, from [56]. White represents the cladding index and red represents the core index.

micron scales, the core and cladding fuse and there is only a single refractive index. Although they have the advantage of a strong evanescent field, one drawback is that these fibers can be quite difficult to work with.

3.2.1 Simulations

Although the side-polished fiber simulation results are not particularly promising for creating a high-efficiency detector, further simulations have revealed that future experiments may build on this technique to create very efficient detectors. It would be very simple in principle to create a bridge detector on one of these fibers, as the dimensions of the fiber are already close to those of a bridge detector, so a deposition of superconductor onto the fiber would create a ready-made detector with no lithography require. These fibers are quite difficult to make and fragile, so great care would need to be taken. However, simulations of detectors made in this way show that it may be a promising future project. My simulations for a 10 nm thick superconducting wire deposited directly onto a tapered fiber give a $1/e$ absorption distance of just 7 microns, meaning that a detector less 100 µm long could have incredibly high efficiency. A side profile of the electromagnetic energy density as the light is absorbed by the detector is shown in Fig. 31. This simulation shows how quickly the light is absorbed over only a few microns.

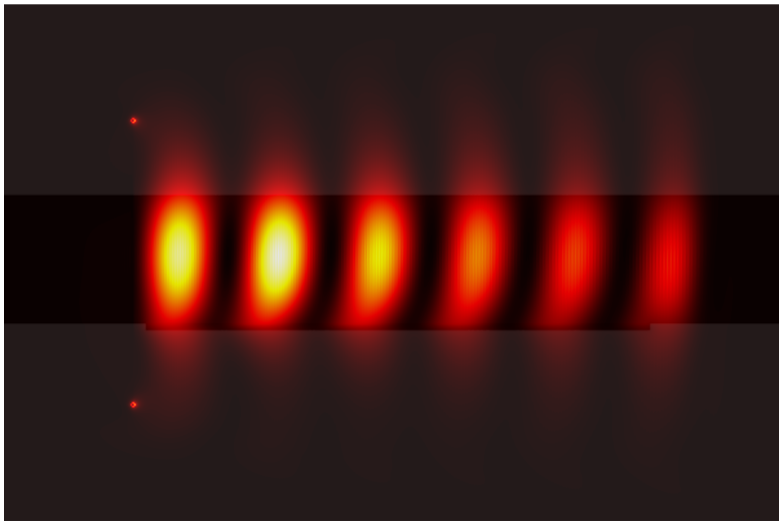

Figure 31: Simulated electromagnetic field density of light being absorbed by a bridge detector on a tapered fiber. The dimensions of the image are 6 µm by 4 µm.

3.3 Future directions

We are still a ways off from demonstrating on-fiber single-photon detectors. There are benefits and drawbacks to pursuing either the side polished fibers or the tapered fibers. It may be best to first demonstrate the effect on side polished fibers while building up the capabilities to make tapered fibers in the background.

For the side polished fibers, the next step is to order custom glass V-grooves that will allow the polished fiber to be secured in the groove for deposition and lithography. It is important to know the exact height of the fiber in the groove so that the height can be input into the EBL system. We also do not have an entirely satisfactory method of aligning the flat side of the fiber with the horizontal. It may be best to find a company that will make the fiber already mounted in a V-groove to get around this issue. I have found a simple mask made of foil works sufficiently well to make the electrical contacts' and the superconductor's

patterns. To connect to the fiber electrically, the easiest way is to use indium, which can be heated slightly with a reflow gun to form a strong connection with the gold contacts without needing wire bonding. The efficiency of any side polished fiber devices will probably be a few percent at most. Using a side-polished fiber with a narrower core and a long (cm or more) detector could have higher efficiency.

For the tapered fibers, we are only starting to consider making these experimentally. The advantage is that a 2 µm diameter fiber could have superconductor deposited on it and potentially form a detector without requiring any lithography. However, tapered fibers can be notoriously difficult to work with and break very easily. Additionally, because the evanescent field is so strong, anything on the surface of the fiber will couple to or scatter the light. This includes not only the superconducting active region, but also any electrical contacts, dust, or superconductor that is not in the active region. So although it would be simple to do this deposition, it is likely that many of the photons will be absorbed or scattered by something other than the detector. There is another concern, which is that depositing on a curved surface will not create a wire of uniform width at the center and edges. Further reading would be required to determine if this would allow vortex detection or not.

In the end, it may be better to choose slightly larger diameter tapered fibers and perform lithography on them. While the lithography would be challenging, the reduced field strength would mean that electrical contacts would not be absorbing as many photons. With a sufficiently wide fiber, it may even be possible to write a U-shaped nanowire detector, so that the electrical contacts are both on one end of the fiber, downstream of the light source, and all photons will have been absorbed by the detector before reaching the contacts. This would, of course, greatly increase the difficulty of electrically connecting to those contacts. There may be an optimal compromise between the low field strength of the side polished fibers and the high field strength of the tapered fibers. This will need to be weighed against the fabrication difficulties, however.

4 Conclusion

Superconducting single-photon detectors are a powerful tool for very high efficiency detection of single-photons over a wide range of wavelengths, and have become a relatively mature technology over the last decade. However, there are still exciting avenues of exploration into the physics and design of these devices.

I have made substantial progress towards being able to fabricate and experiment with superconducting single-photon detectors. We can deposit high quality MoSi and NbN films and electrical contacts, perform electron beam lithography with sub-100 nm line widths and spaces, and etch the films. Additionally, I have characterized much of the process and developed packaging solutions for the finished films.

In addition to this process development, I have also made progress towards vortex-based bridge detectors and on-fiber single-photon detectors. For the bridge detectors, I have designed and written patters for micron-scale bridges based on previous designs in the literature. For the on-fiber single-photon detectors, I have simulated various possible geometries to determine the potential quantum efficiency of these devices.

Going forward, I recommend that the group focuses first on making and characterizing the bridge detectors. Understanding these will likely be critical for producing on-fiber detectors. Additionally, there are interesting experiments that can be done with bridge detectors alone, such as looking for any information that can be learned about the detection even from the electrical signal it produces. The tapered fibers seem like the most promising candidates for near-unity ($> 99\%$) detection efficiency, although there are several technical challenges to overcome. So, in the meantime, it may be best to continue towards making a proof-of-concept device on a side-polished fiber, and potentially looking at fibers with a narrower core.

References

[1] Danilo Bronzi, Federica Villa, Simone Tisa, Alberto Tosi, and Franco Zappa. "SPAD Figures of Merit for Photon-Counting, Photon-Timing, and Imaging Applications: A Review". In: *IEEE Sensors Journal* 16.1 (Jan. 2016), pp. 3–12. ISSN: 1530-437X, 1558-1748, 2379-9153. DOI: 10.1109/JSEN.2015.2483565.

[2] Eric A. Dauler, Matthew E. Grein, Andrew J. Kerman, Francesco Marsili, Shigehito Miki, Sae Woo Nam, Matthew D. Shaw, Hirotaka Terai, Varun B. Verma, and Taro Yamashita. "Review of Superconducting Nanowire Single-Photon Detector System Design Options and Demonstrated Performance". In: *Optical Engineering* 53.8 (June 2014), p. 081907. ISSN: 0091-3286. DOI: 10.1117/1.OE.53.8.081907.

[3] Yu P. Korneeva, M. Yu Mikhailov, Yu P. Pershin, N. N. Manova, A. V. Divochiy, Yu B. Vakhtomin, A. A. Korneev, K. V. Smirnov, A. G. Sivakov, A. Yu Devizenko, and G. N. Goltsman. "Superconducting Single-Photon Detector Made of MoSi Film". In: *Superconductor Science and Technology* 27.9 (Aug. 2014), p. 095012. ISSN: 0953-2048. DOI: 10.1088/0953-2048/27/9/095012.

[4] Shi-Zeng Lin, Oscar Ayala-Valenzuela, Ross D. McDonald, Lev N. Bulaevskii, Terry G. Holesinger, Filip Ronning, Nina R. Weisse-Bernstein, Todd L. Williamson, Alexander H. Mueller, Mark A. Hoffbauer, Michael W. Rabin, and Matthias J. Graf. "Characterization of the Thin-Film NbN Superconductor for Single-Photon Detection by Transport Measurements". In: *Physical Review B* 87.18 (May 2013), p. 184507. DOI: 10.1103/PhysRevB.87.184507.

[5] J. J. Olaya, L. Huerta, S. E. Rodil, and R. Escamilla. "Superconducting Niobium Nitride Films Deposited by Unbalanced Magnetron Sputtering". In: *Thin Solid Films* 516.23 (Oct. 2008), pp. 8768–8773. ISSN: 0040-6090. DOI: 10.1016/j.tsf.2008.06.065.

[6] Y. M. Shy, L. E. Toth, and R. Somasundaram. "Superconducting Properties, Electrical Resistivities, and Structure of NbN Thin Films". In: *Journal of Applied Physics* 44.12 (Dec. 1973), pp. 5539–5545. ISSN: 0021-8979. DOI: 10.1063/1.1662193.

[7] Archan Banerjee, Luke J Baker, Alastair Doye, Magnus Nord, Robert M Heath, Kleanthis Erotokritou, David Bosworth, Zoe H Barber, Ian MacLaren, and Robert H Hadfield. "Characterisation of Amorphous Molybdenum Silicide (MoSi) Superconducting Thin Films and Nanowires". In: *Superconductor Science and Technology* 30.8 (Aug. 2017), p. 084010. ISSN: 0953-2048, 1361-6668. DOI: 10.1088/1361-6668/aa76d8.

[8] Michael Tinkham. *Introduction to Superconductivity*. 2. ed. Dover Books on Physics. OCLC: 728146785. Mineola, NY: Dover Publ, 2004. ISBN: 978-0-486-43503-9.

[9] A. A. Abrikosov. *Fundamentals of the Theory of Metals*. Open Library ID: OL2241442M. Amsterdam, New York, New York, NY, USA: North-Holland, 1988. ISBN: 978-0-444-87094-0 978-0-444-87095-7.

[10] Kyle DeBry and Gregory Lafyatis. "Note: Electroplating Process for Connectorizing Superconducting NbTi Cables". In: *Review of Scientific Instruments* 89.7 (July 2018), p. 076108. ISSN: 0034-6748. DOI: 10.1063/1.5030431.

[11] G. Bergmann. "Amorphous Metals and Their Superconductivity". In: *Physics Reports* 27.4 (Sept. 1976), pp. 159–185. ISSN: 0370-1573. DOI: 10.1016/0370-1573(76)90040-5.

[12] W. Buckel and R. Hilsch. "Einfluß der Kondensation bei tiefen Temperaturen auf den elektrischen Widerstand und die Supraleitung für verschiedene Metalle". In: *Zeitschrift für Physik* 138.2 (Apr. 1954), pp. 109–120. ISSN: 0044-3328. DOI: 10.1007/BF01337903.

[13] C. C. Tsuei. "Amorphous Superconductors". In: *Superconductor Materials Science: Metallurgy, Fabrication, and Applications*. Ed. by Simon Foner and Brian B. Schwartz. NATO Advanced Study Institutes Series. Boston, MA: Springer US, 1981, pp. 735–756. ISBN: 978-1-4757-0037-4. DOI: 10.1007/978-1-4757-0037-4_12.

[14] Zhao Zhong-xian, Meng Ru-ling, Zhou Ping, and Li Lin. "Amorphous Phase Formation of Mo 1-x Ge x , Mo 1-x Si x Films and Their Superconducting Properties". In: *Chinese Physics Letters* 1.1 (Aug. 1984), pp. 23–26. ISSN: 0256-307X. DOI: 10.1088/0256-307X/1/1/007.

[15] V. B. Verma, B. Korzh, F. Bussières, R. D. Horansky, S. D. Dyer, A. E. Lita, I. Vayshenker, F. Marsili, M. D. Shaw, H. Zbinden, R. P. Mirin, and S. W. Nam. "High-Efficiency Superconducting Nanowire Single-Photon Detectors Fabricated from MoSi Thin-Films". In: *Optics Express* 23.26 (Dec. 2015), p. 33792. ISSN: 1094-4087. DOI: 10.1364/OE.23.033792.

[16] D. Bosworth, S.-L. Sahonta, R. H. Hadfield, and Z. H. Barber. "Amorphous Molybdenum Silicon Superconducting Thin Films". In: *AIP Advances* 5.8 (Aug. 2015), p. 087106. ISSN: 2158-3226. DOI: 10.1063/1.4928285.

[17] Gil Bachar, Ilya Baskin, Oleg Shtempluck, and Eyal Buks. "Superconducting Nanowire Single Photon Detectors On-Fiber". In: *Applied Physics Letters* 101.26 (Dec. 2012), p. 262601. ISSN: 0003-6951, 1077-3118. DOI: 10.1063/1.4773305.

[18] Alex D. Semenov, Gregory N. Gol'tsman, and Alexander A. Korneev. "Quantum Detection by Current Carrying Superconducting Film". In: *Physica C: Superconductivity* 351.4 (Apr. 2001), pp. 349–356. ISSN: 09214534. DOI: 10.1016/S0921-4534(00)01637-3.

[19] W. J. Skocpol, M. R. Beasley, and M. Tinkham. "Self-heating Hotspots in Superconducting Thin-film Microbridges". In: *Journal of Applied Physics* 45.9 (Sept. 1974), pp. 4054–4066. ISSN: 0021-8979. DOI: 10.1063/1.1663912.

[20] A. M. Kadin and M. W. Johnson. "Nonequilibrium Photon-induced Hotspot: A New Mechanism for Photodetection in Ultrathin Metallic Films". In: *Applied Physics Letters* 69.25 (Dec. 1996), pp. 3938–3940. ISSN: 0003-6951. DOI: 10.1063/1.117576.

[21] Andrew J. Kerman, Eric A. Dauler, William E. Keicher, Joel K. W. Yang, Karl K. Berggren, G. Gol'tsman, and B. Voronov. "Kinetic-Inductance-Limited Reset Time of Superconducting Nanowire Photon Counters". In: *Applied Physics Letters* 88.11 (Mar. 2006), p. 111116. ISSN: 0003-6951. DOI: 10.1063/1.2183810.

[22] G. N. Gol'tsman, O. Okunev, G. Chulkova, A. Lipatov, A. Semenov, K. Smirnov, B. Voronov, A. Dzardanov, C. Williams, and Roman Sobolewski. "Picosecond Superconducting Single-Photon Optical Detector". In: *Applied Physics Letters* 79.6 (Aug. 2001), pp. 705–707. ISSN: 0003-6951. DOI: 10.1063/1.1388868.

[23] Dileep V. Reddy, Adriana E. Lita, Sae Woo Nam, Richard P. Mirin, and Varun B. Verma. "Achieving 98% System Efficiency at 1550 Nm in Superconducting Nanowire Single Photon Detectors". In: *Rochester Conference on Coherence and Quantum Optics (CQO-11)*. Rochester, New York: OSA, 2019, W2B.2. ISBN: 978-1-943580-69-9. DOI: 10.1364/CQO.2019.W2B.2.

[24] Clinton Cahall, Kathryn L. Nicolich, Nurul T. Islam, Gregory P. Lafyatis, Aaron J. Miller, Daniel J. Gauthier, and Jungsang Kim. "Multi-Photon Detection Using a Conventional Superconducting Nanowire Single-Photon Detector". In: *Optica* 4.12 (Dec. 2017), pp. 1534–1535. ISSN: 2334-2536. DOI: 10.1364/OPTICA.4.001534.

[25] Kathryn L. Nicolich, Clinton Cahall, Nurul T. Islam, Gregory P. Lafyatis, Jungsang Kim, Aaron J. Miller, and Daniel J. Gauthier. "Universal Model for the Turn-On Dynamics of Superconducting Nanowire Single-Photon Detectors". In: *Physical Review Applied* 12.3 (Sept. 2019), p. 034020. ISSN: 2331-7019. DOI: 10.1103/PhysRevApplied.12.034020.

[26] Aaron J. Miller, Adriana E. Lita, Brice Calkins, Igor Vayshenker, Steven M. Gruber, and Sae Woo Nam. "Compact Cryogenic Self-Aligning Fiber-to-Detector Coupling with Losses below One Percent". In: *Optics Express* 19.10 (May 2011), p. 9102. ISSN: 1094-4087. DOI: 10.1364/OE.19.009102.

[27] L. Ceccarelli, D. Vasyukov, M. Wyss, G. Romagnoli, N. Rossi, L. Moser, and M. Poggio. "Imaging Pinning and Expulsion of Individual Superconducting Vortices in Amorphous MoSi Thin Films". In: *Physical Review B* 100.10 (Sept. 2019), p. 104504. DOI: 10.1103/PhysRevB.100.104504.

[28] A. N. Zotova and D. Y. Vodolazov. "Photon Detection by Current-Carrying Superconducting Film: A Time-Dependent Ginzburg-Landau Approach". In: *Physical Review B* 85.2 (Jan. 2012), p. 024509. ISSN: 1098-0121, 1550-235X. DOI: 10.1103/PhysRevB.85.024509.

[29] D. Yu. Vodolazov. "Single-Photon Detection by a Dirty Current-Carrying Superconducting Strip Based on the Kinetic-Equation Approach". In: *Physical Review Applied* 7.3 (Mar. 2017), p. 034014. ISSN: 2331-7019. DOI: 10.1103/PhysRevApplied.7.034014.

[30] Yu. P. Korneeva, D. Yu. Vodolazov, A. V. Semenov, I. N. Florya, N. Simonov, E. Baeva, A. A. Korneev, G. N. Goltsman, and T. M. Klapwijk. "Optical Single-Photon Detection in Micrometer-Scale NbN Bridges". In: *Physical Review Applied* 9.6 (June 2018), p. 064037. ISSN: 2331-7019. DOI: 10.1103/PhysRevApplied.9.064037.

[31] Anand Kamlapure, Mintu Mondal, Madhavi Chand, Archana Mishra, John Jesudasan, Vivas Bagwe, L. Benfatto, Vikram Tripathi, and Pratap Raychaudhuri. "Measurement of Magnetic Penetration Depth and Superconducting Energy Gap in Very Thin Epitaxial NbN Films". In: *Applied Physics Letters* 96.7 (Feb. 2010), p. 072509. ISSN: 0003-6951. DOI: 10.1063/1.3314308.

[32] Yu. P. Korneeva, N.N. Manova, I.N. Florya, M. Yu. Mikhailov, O.V. Dobrovolskiy, A.A. Korneev, and D. Yu. Vodolazov. "Different Single-Photon Response of Wide and Narrow Superconducting Mo x Si 1 - x Strips". In: *Physical Review Applied* 13.2 (Feb. 2020), p. 024011. ISSN: 2331-7019. DOI: 10.1103/PhysRevApplied.13.024011.

[33] R. Lusche, A. Semenov, K. Ilin, M. Siegel, Y. Korneeva, A. Trifonov, A. Korneev, G. Goltsman, D. Vodolazov, and H.-W. Hübers. "Effect of the Wire Width on the Intrinsic Detection Efficiency of Superconducting-Nanowire Single-Photon Detectors". In: *Journal of Applied Physics* 116.4 (July 2014), p. 043906. ISSN: 0021-8979, 1089-7550. DOI: 10.1063/1.4891105.

[34] P. J Kelly and R. D Arnell. "Magnetron Sputtering: A Review of Recent Developments and Applications". In: *Vacuum* 56.3 (Mar. 2000), pp. 159–172. ISSN: 0042-207X. DOI: 10.1016/S0042-207X(99)00189-X.

[35] J. O. Choi, J. A. Moore, J. C. Corelli, J. P. Silverman, and H. Bakhru. "Degradation of Poly(Methylmethacrylate) by Deep Ultraviolet, X-ray, Electron Beam, and Proton Beam Irradiations". In: *Journal of Vacuum Science & Technology B: Microelectronics Processing and Phenomena* 6.6 (Nov. 1988), pp. 2286–2289. ISSN: 0734-211X. DOI: 10.1116/1.584071.

[36] Bärbel Krause, Gregory Abadias, Anny Michel, Peter Wochner, Shyjumon Ibrahimkutty, and Tilo Baumbach. "Direct Observation of the Thickness-Induced Crystallization and Stress Build-Up during Sputter-Deposition of Nanoscale Silicide Films". In: *ACS Applied Materials & Interfaces* 8.50 (Dec. 2016), pp. 34888–34895. ISSN: 1944-8244, 1944-8252. DOI: 10.1021/acsami.6b12413.

[37] Twisp. *Wafer Flats Convention V2*. URL: https://commons.wikimedia.org/wiki/File:Wafer%5C_flats%5C_convention%5C_v2.svg.

[38] Georgia Tech. *Nanolithography/Electron Beam Lithography*. URL: http://nanolithography.gatech.edu/processes.html.

[39] Kristine M. Rosfjord, Joel K. W. Yang, Eric A. Dauler, Andrew J. Kerman, Vikas Anant, Boris M. Voronov, Gregory N. Gol'tsman, and Karl K. Berggren. "Nanowire Single-Photon Detector with an Integrated Optical Cavity and Anti-Reflection Coat-

ing". In: *Optics Express* 14.2 (Jan. 2006), pp. 527–534. ISSN: 1094-4087. DOI: 10.1364/OPEX.14.000527.

[40] Sung-Wook Nam, Michael J. Rooks, Joel K. W. Yang, Karl K. Berggren, Hyun-Mi Kim, Min-Hyun Lee, Ki-Bum Kim, Jae Hwan Sim, and Do Yeung Yoon. "Contrast Enhancement Behavior of Hydrogen Silsesquioxane in a Salty Developer". In: *Journal of Vacuum Science & Technology B: Microelectronics and Nanometer Structures* 27.6 (2009), p. 2635. ISSN: 10711023. DOI: 10.1116/1.3245991.

[41] Kyle DeBry. *Kyledebry/DetectorGDS*. Apr. 2020. URL: https://github.com/kyledebry/DetectorGDS.

[42] T. H. P. Chang. "Proximity Effect in Electron-beam Lithography". In: *Journal of Vacuum Science and Technology* 12.6 (Nov. 1975), pp. 1271–1275. ISSN: 0022-5355. DOI: 10.1116/1.568515.

[43] Mihir Parikh. "Corrections to Proximity Effects in Electron Beam Lithography. I. Theory". In: *Journal of Applied Physics* 50.6 (June 1979), pp. 4371–4377. ISSN: 0021-8979. DOI: 10.1063/1.326423.

[44] John R. Clem and Karl K. Berggren. "Geometry-Dependent Critical Currents in Superconducting Nanocircuits". In: *Physical Review B* 84.17 (Nov. 2011), p. 174510. ISSN: 1098-0121, 1550-235X. DOI: 10.1103/PhysRevB.84.174510.

[45] George Harman. *Wire Bonding in Microelectronics, 3/E*. 3 edition. New York: McGraw-Hill Education, Feb. 2010. ISBN: 978-0-07-147623-2.

[46] Farhad Farassat and Walter Birgel. "Ball Bonding Method and Apparatus for Performing the Method". US4925083A. May 1990.

[47] Xiaolong Hu, C.W. Holzwarth, D. Masciarelli, E.A. Dauler, and K.K. Berggren. "Efficiently Coupling Light to Superconducting Nanowire Single-Photon Detectors". In: *IEEE Transactions on Applied Superconductivity* 19.3 (June 2009), pp. 336–340. ISSN: 1051-8223, 1558-2515. DOI: 10.1109/TASC.2009.2018035.

[48] Shigehito Miki, Taro Yamashita, Mikio Fujiwara, Masahide Sasaki, and Zhen Wang. "Characterization of Coupling Efficiency and Absorption Coefficient for Fiber-Coupled SNSPD With an Optical Cavity". In: *IEEE Transactions on Applied Superconductivity* 21.3 (June 2011), pp. 332–335. ISSN: 1051-8223, 1558-2515. DOI: 10.1109/TASC.2010.2091486.

[49] A Engel. "Comment on 'Superconducting Transition in Nb Nanowires Fabricated Using a Focused-Ion Beam'". In: *Nanotechnology* 21.16 (Apr. 2010), p. 168001. ISSN: 0957-4484, 1361-6528. DOI: 10.1088/0957-4484/21/16/168001.

[50] Shiao-Min Tseng and Chin-Lin Chen. "Side-Polished Fibers". In: *Applied Optics* 31.18 (June 1992), p. 3438. ISSN: 0003-6935, 1539-4522. DOI: 10.1364/AO.31.003438.

[51] Anna.Og. Dikovska, P.A. Atanasov, A.Ts. Andreev, B.S. Zafirova, E.I. Karakoleva, and T.R. Stoyanchov. "ZnO Thin Film on Side Polished Optical Fiber for Gas Sensing Applications". In: *Applied Surface Science* 254.4 (Dec. 2007), pp. 1087–1090. ISSN: 01694332. DOI: 10.1016/j.apsusc.2007.07.155.

[52] T. Sherwood, A.C. Young, J. Takayesu, A.K.Y. Jen, L.R. Dalton, and Antao Chen. "Microring Resonators on Side-Polished Optical Fiber". In: *IEEE Photonics Technology Letters* 17.10 (Oct. 2005), pp. 2107–2109. ISSN: 1041-1135. DOI: 10.1109/LPT.2005.854405.

[53] Phoenix Photonics. *Side Polished Optical Fibers*. URL: http://www.phoenixphotonics.com/website/technology/side-polished-fibers.html.

[54] MIT. *Manual*. URL: https://meep.readthedocs.io/en/latest/.

[55] Kyle DeBry. *Kyledebry/Evan*. Nov. 2019. URL: https://github.com/kyledebry/Evan.

[56] Y. Mustapha Kamil, M. H. Abu Bakar, M. A. Mustapa, M. H. Yaacob, A. Syahir, and M. A. Mahdi. "Sensitive and Specific Protein Sensing Using Single-Mode Tapered

Fiber Immobilized With Biorecognition Molecules". In: *IEEE Photonics Journal* 7.6 (Dec. 2015), pp. 1–9. ISSN: 1943-0655. DOI: 10.1109/JPHOT.2015.2490486.

[57] Jacques Bures and René Ghosh. "Power Density of the Evanescent Field in the Vicinity of a Tapered Fiber". In: *JOSA A* 16.8 (Aug. 1999), pp. 1992–1996. ISSN: 1520-8532. DOI: 10.1364/JOSAA.16.001992.